



Cite this: *Phys. Chem. Chem. Phys.*, 2025, 27, 9522

## Reactions of fluid and lattice oxygen mediated by interstitial atoms at the $\text{TiO}_2(110)$ –water interface†

Heonjae Jeong, <sup>bc</sup> Ian I. Suni, <sup>a</sup> Raylin Chen, <sup>a</sup> Marina Miletic, <sup>a</sup> Xiao Su <sup>a</sup> and Edmund G. Seebauer <sup>\*a</sup>

$\text{O}_2$  interacts with  $\text{TiO}_2$  surfaces in numerous aqueous reactions for clean hydrogen production, wastewater cleanup, reduction of  $\text{CO}_2$  and  $\text{N}_2$ , and  $\text{O}_2$  sensing. In many cases, these reactions involve reversible exchange of O with the solid, whose participation is usually thought to require oxygen vacancies ( $\text{V}_\text{O}$ ). Based on measurements of oxygen isotopic self-diffusion in rutile  $\text{TiO}_2$  under water, this work proposes a different perspective centered on O interstitial atoms ( $\text{O}_\text{i}$ ). Experiments with varying concentrations of  $\text{O}_2$  and mole fractions of  $^{18}\text{O}$  show that the (110) surface facilitates O exchange with both the  $\text{H}_2\text{O}$  liquid and its dissolved  $\text{O}_2$ . First-principles calculations indicate that on-top and “surface  $\text{O}_\text{i}$ ” configurations of adsorbed O participate sequentially in the exchange process. Adsorbed OH appears to provide a single pathway for  $\text{H}_2\text{O}$  and  $\text{O}_2$  to contribute oxygen, although fitting the diffusion data to simple models indicates that  $\text{H}_2\text{O}$  contributes more. Because rutile  $\text{TiO}_2$  is a prototypical metal oxide, this picture based on  $\text{O}_\text{i}$  probably generalizes in many cases to other oxides – explaining important aspects of their thermal, electrochemical, and photochemical reactions with dissolved  $\text{O}_2$ .

Received 23rd January 2025,  
Accepted 5th April 2025

DOI: 10.1039/d5cp00319a

rsc.li/pccp

## 1. Introduction

$\text{O}_2$  interacts with water-submerged  $\text{TiO}_2$  surfaces in many aqueous reactions for production of clean hydrogen,<sup>1–5</sup> cleanup of wastewater,<sup>6–11</sup> reduction of  $\text{N}_2$  to  $\text{NH}_3$ ,<sup>12–16</sup> reduction of  $\text{CO}_2$  to hydrocarbons,<sup>17,18</sup> production of  $\text{H}_2\text{O}_2$ ,<sup>19</sup> and sensing of  $\text{O}_2$ .<sup>20</sup> For the oxygen evolution reaction (OER) by photocatalysis<sup>21,22</sup> and electrocatalysis,<sup>23</sup> significant attention focuses on participation of lattice oxygen from  $\text{TiO}_2$ . This attention extends to other metal oxides<sup>24–28</sup> for the OER, the oxygen reduction reaction<sup>29–31</sup> (ORR) and advanced oxidation processes (AOP).<sup>11</sup> Many authors use the term “lattice oxygen

mechanism” (LOM) to describe the chemical pathways for exchange of atoms between  $\text{O}_2$  and the solid,<sup>21–23,25–27,32,33</sup> although “Mars–van Krevelen mechanism” prevails among other authors.<sup>31,34</sup> Such mechanisms contrast with pathways involving atoms derived only from the liquid, termed an “adsorbate evolution mechanism” in the OER.<sup>10,26,35</sup>

Regardless of the oxide or driving force (thermal, electrochemical, or photochemical), O vacancies ( $\text{V}_\text{O}$ ) are usually thought to mediate participation of lattice oxygen.<sup>25,27,33,35</sup> However, this physical picture has been questioned recently,<sup>29</sup> partly because O interstitial atoms ( $\text{O}_\text{i}$ ) appear to facilitate lattice O participation in some cases.<sup>29,30</sup> This literature struggles to reconcile the notion of “active oxygen” in the lattice with the assumed need for surface  $\text{V}_\text{O}$  to assist the reaction. Furthermore, mediation by vacancies contains implicit inconsistencies. For example, the OER on  $\text{TiO}_2$  and perovskites often operates under intensely oxidizing conditions<sup>26,35</sup> (strongly alkaline pH, high applied potential, and high  $\text{O}_2$  concentration) that are not hospitable for surface  $\text{V}_\text{O}$ , which reflect chemical reduction. Moreover, increasing the  $\text{V}_\text{O}$  concentration in O-deficient perovskites increases the barrier for participation of lattice O.<sup>26</sup> In other words, the reaction seems to require vacancies, yet increasing their concentration diminishes the rate (e.g., in  $\text{SrCoO}_3$ ).<sup>36</sup>

As described elsewhere,<sup>29,30</sup> an alternate perspective based on  $\text{O}_\text{i}$  merits consideration in many cases. Under O-rich

<sup>a</sup> Department of Chemical and Biomolecular Engineering, University of Illinois at Urbana-Champaign, Urbana, Illinois 61801, USA. E-mail: eseebauer@illinois.edu

<sup>b</sup> Department of Mechanical Science and Engineering, University of Illinois at Urbana-Champaign, Urbana, Illinois 61801, USA

<sup>c</sup> Department of Electronic Engineering, Gachon University, Seongnam, Gyeonggi 13120, South Korea

† Electronic supplementary information (ESI) available: Method for determination of profile metrics; statistical analysis example calculation; adsorption models (linear and dual pathway); table of surface coverages of  $^{18}\text{O}$  and  $^{16}\text{O}$ ; additional supplementary figures and tables including change in pH vs.  $\ln(F_{18})$ , profile metrics vs. applied potential  $V_{\text{appl}}$ ,  $F$ -tests for null hypothesis on slopes of profile metrics vs.  $V_{\text{appl}}$ , histograms of the five profile metrics at 70 °C with and without applied bias, atomic geometries of  $\text{TiO}_2(110)$  with and without adsorbed bridging hydroxyls, adsorption energy and Bader charge of adsorbed O on  $\text{TiO}_2(110)$  under Ti-rich conditions. See DOI: <https://doi.org/10.1039/d5cp00319a>



conditions,  $O_i$  mediates O exchange between several different binary oxides and liquid  $H_2O$ .<sup>37,38</sup> Yet no physical picture has been proposed by which O atoms transfer between the lattice, diffusing  $O_i$ , the surface, and dissolved  $O_2$ .

The mediating form of adsorbed O remains especially murky. Adsorbed OH (anion and neutral) and molecular  $H_2O$  dominate adsorbate populations on submerged metal oxides,<sup>39–42</sup> but reaction mechanisms for  $O_2$  atop oxides assume participation of adsorbed O,<sup>35</sup> whose existence has been inferred from experiments and density functional theory (DFT) calculations.<sup>43–48</sup> The literature for catalysis and surface science considers O on rutile  $TiO_2$  to sit directly atop a metal cation.<sup>49–56</sup> This species protonates readily. In contrast, DFT calculations for three different oxides<sup>37,57,58</sup> reveal a “surface interstitial” that converts into bulk  $O_i$  by diffusive hopping. The surface interstitial’s high bond coordination implies little propensity for protonation.

Interconversion between these forms of adsorbed O provides the foundation for a self-consistent physical picture to describe atom exchange between the lattice and dissolved  $O_2$ . To support this picture, the present work employs isotopic self-diffusion measurements in submerged rutile  $TiO_2(110)$  single crystals with varying concentrations of  $^{18}O$  isotopic label. We selected the (110) surface termination because extensive literature already exists for this orientation, and its nonpolar structure should minimize surface reconstruction upon immersion.<sup>59</sup> These experiments show that O exchanges between the solid and both dissolved  $O_2$  and  $H_2O$  liquid, mediated within the solid by  $O_i$ . At the surface, DFT calculations suggest that adsorbed O exists in both on-top and surface interstitial configurations. Adsorbed OH appears to provide a single pathway for  $H_2O$  and  $O_2$  to contribute oxygen, although fitting the diffusion data to simple models indicates that  $H_2O$  contributes more. Because rutile  $TiO_2$  is a prototypical metal oxide,<sup>39,60</sup> this picture based on  $O_i$  probably generalizes in many cases to other oxides – explaining important aspects of their thermal, electrochemical, and photochemical reactions with dissolved  $O_2$ .

## 2. Methods

### 2.1 Experiments

Many published experiments seeking to measure participation of lattice O have focused on detecting  $^{18}O$  in the fluid or on the solid surface.<sup>24,32,61</sup> In contrast, the present work focuses on measuring  $^{18}O$  self-diffusion within the solid. Such measurements offer a complementary perspective more directly attuned to defect behavior. Our protocols for the  $^{18}O$  self-diffusion experiments have been detailed previously.<sup>37</sup> The experiments were performed at varying temperatures involving no photochemical perturbations. Undoped single-crystal rutile  $TiO_2(110)$  specimens ( $5 \times 5 \times 0.5$  mm) purchased from MTI Corp. were de-greased by 10 min of ultrasonic agitation in a succession of solvents (acetone, isopropanol, ethanol, and methanol) followed by wet etching (1:2, 30%  $NH_4OH:H_2O$ ) at room temperature for 40 min to remove elemental poisons that inhibit  $O_i$  injection. Surface analysis by X-ray photoelectron spectroscopy

(XPS) showed only Ti, O, and C within the detection limit, both before and after  $O_i$  diffusion. Consistent with previous studies, no variations in surface composition with experimental conditions were observed. Atomic force microscopy (AFM) revealed a root mean square (rms) roughness of  $0.23 \pm 0.03$  nm for as-received  $TiO_2$  and  $0.14 \pm 0.08$  nm after wet etching.<sup>58</sup>

We discovered empirically that, during submersion in water, application of potential bias in a conventional three-electrode cell configuration increases the  $O_i$  injection rate and thereby aids the measurement of profile metrics.  $TiO_2$  specimens were immersed for 60 min at constant temperature ( $70^\circ C$ ) with a potential bias applied using a Biologic SP200 potentiostat. The electrical connection to the  $TiO_2$  specimens was a Cu wire attached with double-stick carbon tape covered with Kapton. An Ag/AgCl reference electrode and a Pt counter electrode were employed. The water contained no electrolyte, and the pH was about 7. Before immersion, 10 min of gas bubbling through the aqueous solution with simultaneous gas flow through the headspace established liquid–gas equilibrium.

The solid  $TiO_2$  was undoped and assumed to be insulating. In addition, no electrolyte was employed, so no faradaic electrochemistry occurred during the experiments. Potentiostat measurements of the current were very small (10–100 nA) and uncorrelated with any profile metric. The potentiostat itself typically displayed an overload warning characteristic of an open circuit. As shown in Fig. S1 of the ESI,† measurements of pH before and after each self-diffusion experiment revealed only small changes. The starting pH averaged 6.96 with a standard deviation of 0.30, and the pH change during diffusion was most commonly 0.25 or less.

In water submersion without applied bias, injected fluxes of  $O_i$  are sufficiently high to yield isotopic fractionation within the first few nanometers of the surface.<sup>38</sup> In this region, the concentration of  $^{18}O$  dips below the natural abundance level – a counterintuitive phenomenon, because the ambient solution is enriched in  $^{18}O$ . Fractionation originates from high gradients in O concentration combined with the statistics of diffusion by an interstitial mechanism, wherein two O atoms share a single lattice site and either atom can hop into an adjacent site in a diffusive event. The existence of fractionation provides added features in the diffusion profiles for quantifying profile behavior.

To ascertain the relative contributions of  $O_2$  and  $H_2O$  to injection and diffusion of  $O_i$ , the following combinations of isotopic labels and water–gas ambient were investigated:

- Case I: 10%  $^{18}O$ -labeled  $H_2O$  (Sigma-Aldrich), natural abundance  $N_2$  (19 profiles)
- Case II: 10%  $^{18}O$ -labeled  $H_2O$ , natural abundance  $O_2$  (8 profiles)
- Case III: 10%  $^{18}O$ -labeled  $H_2O$ , natural abundance air (74 profiles)
- Case IV: natural O-abundance (0.2%)  $D_2O$  (Sigma-Aldrich), 97% labeled  $^{18}O_2$  (Sigma-Aldrich, 12 profiles)

These four cases contain differing concentrations of  $^{18}O$  in the liquid and gas phases, allowing inference of the source of  $^{18}O$ .



$^{18}\text{O}$  concentration profiles were measured *ex situ* by secondary ion mass spectrometry (SIMS) in time-of-flight mode using a PHI-TRIFT III instrument with a 3 keV Cs ion beam source and a spot size of 0.5 mm.  $^{18}\text{O}$  concentrations were calibrated to the known natural abundance of  $^{18}\text{O}$  (0.2%) in the as-received  $\text{TiO}_2$  specimens. Profiles were measured at 2–5 different locations on the surface of each specimen.

## 2.2 DFT calculations

DFT calculations were performed using the Vienna *Ab Initio* Simulation Package (VASP).<sup>62,63</sup> The bulk rutile  $\text{TiO}_2$  structure was obtained from the Materials Project.<sup>64</sup> The structure was optimized using the Perdew–Burke–Ernzerhof<sup>65</sup> (PBE) generalized gradient approximation (GGA) exchange–correlation functional, and the projector augmented wave<sup>66</sup> (PAW) method was employed. Details of the optimized structure were previously published.<sup>67</sup> For the slab modeling, the (110) plane in its  $2 \times 1$  *in vacuo* reconstruction was employed. Some computational evidence suggests the surface reconstructs to  $1 \times 1$  periodicity upon submersion,<sup>68</sup> but most first principles simulations of this surface upon submersion continue to employ the  $2 \times 1$  structure.<sup>46,56</sup> A plane wave cutoff energy of 520 eV was used, together with Monkhorst–Pack  $k$ -point sampling having a  $4 \times 4 \times 1$  mesh size. All atoms were relaxed until the forces on each atom were smaller than 0.01 eV  $\text{\AA}^{-1}$ . The slab thickness was set to 15.74  $\text{\AA}$  and included five trilayers of ( $\text{O}-\text{Ti}_2\text{O}_2-\text{O}$ ) to allow for a net charge-neutral stoichiometry.<sup>57</sup> A vacuum thickness of 15.0  $\text{\AA}$  was employed to isolate each slab from its images originating from periodic boundary conditions.

To model specific adsorption cases, all potential adsorption sites were examined. The (110) plane includes  $\text{Ti}_{5\text{f}}$ ,  $\text{O}_{3\text{f}}$  and  $\text{O}_{2\text{f}}$  sites, although only the first two lie in-plane and are of direct concern here. Adsorbed O atoms adopt an “on-top” geometry at the  $\text{Ti}_{5\text{f}}$  site. At the  $\text{O}_{3\text{f}}$  site, adsorbed O atoms can adopt a “dumbbell” geometry (neutral charge) containing an O–O bond or a “split” geometry (–2 charge) that contains bonds only to surrounding metal cations. For the split, we employed a previous protocol<sup>57</sup> that places an O vacancy on the backside of the slab to facilitate adsorbate charging while maintaining the simulation’s Fermi energy ( $E_F$ ) at the top of the valence band. The adsorption energy was computed as described previously,<sup>57</sup> with the oxygen chemical potential computed under standard conditions (25 °C and 1 atm) for both O-rich ( $\mu_{\text{O}} = -4.68$  eV) and Ti-rich ( $\mu_{\text{O}} = -10.11$  eV) environments.

## 3. Results

Fig. 1 illustrates typical  $^{18}\text{O}$  SIMS profiles following diffusion. The general features match those observed previously in the absence of applied potential bias,<sup>37,38</sup> with the most dramatic being the isotopic fractionation represented by the near-surface “valley” wherein the  $^{18}\text{O}$  concentration drops well below natural abundance ( $C_{\text{nat}} = 1.29 \times 10^{20} \text{ cm}^{-3}$ ) as described at length elsewhere.<sup>38</sup> This phenomenon is transient and represents a manifestation of uphill diffusion<sup>69</sup> in the solid state.

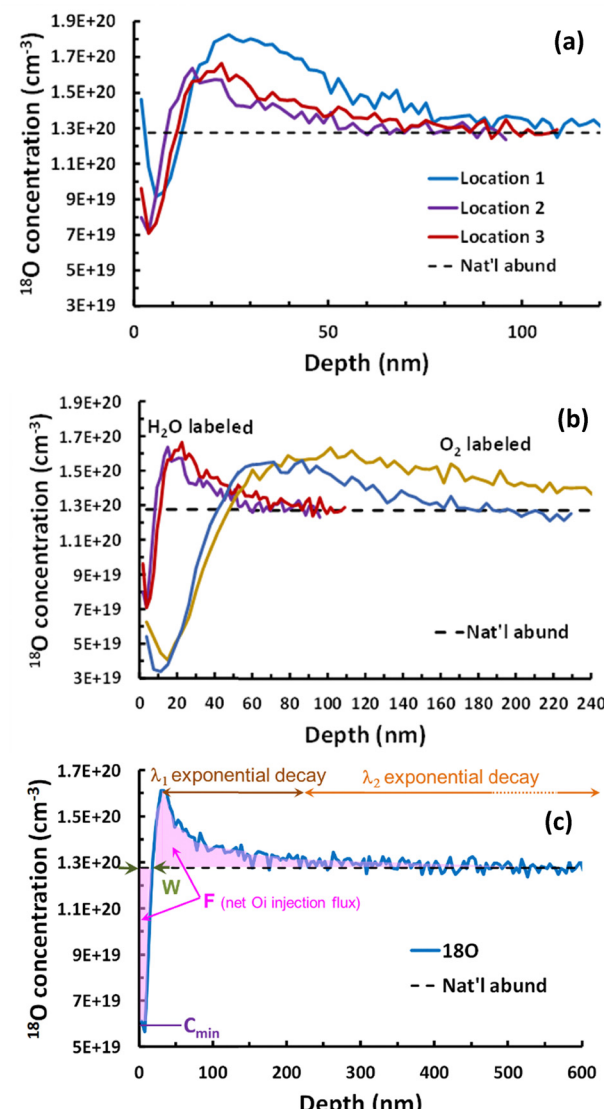


Fig. 1 (a) Example  $^{18}\text{O}$  profiles at several locations on a single specimen of case II ( $\text{H}_2\text{O}$  with 10 at%  $^{18}\text{O}$ ) with  $V_{\text{appl}} = -0.8$  V vs. Ag/AgCl, 70 °C,  $t = 60$  min, illustrating “valley” regions (having  $^{18}\text{O}$  concentrations below natural abundance). The variability is characteristic as discussed in the text. (b) Example  $^{18}\text{O}$  profiles comparing case II (“ $\text{H}_2\text{O}$  labeled,” 10 at%  $^{18}\text{O}$ ) and case IV (“ $\text{O}_2$  labeled,” 97 at%  $^{18}\text{O}$ ) at 70 °C,  $t = 60$  min. Although  $V_{\text{appl}}$  varies, this condition does not affect the profiles; the variation has the same origin as in (a). Typical  $\text{O}_2$ -labeled profiles extend much deeper than  $\text{H}_2\text{O}$ -labeled profiles and exhibit deeper and wider valleys near the surface. (c) Example profile showing definitions of the metrics  $W$  and  $C_{\text{min}}$ ,  $F_{18}$ ,  $\lambda_1$  and  $\lambda_2$ . Profile was measured in air (case I) at  $V_{\text{appl}} = -0.4$  V, 70 °C,  $t = 60$  min. For all profiles here, the water contained no electrolyte, and was air-equilibrated prior to diffusion by bubbling for 10 min.

All features are stable during long-term storage. Fig. 1a shows examples of profiles for labeled water with natural abundance  $\text{O}_2$  (case II). Details of the profile shapes vary with position on a given specimen. Such variations have been discussed at length elsewhere<sup>58,70</sup> and arise in large part from differences in the level of surface contamination, especially adventitious carbon, which can poison the surface sites that facilitate injection. Fig. 1b shows typical profiles comparing



cases II and IV, wherein the gas ambient is pure  $O_2$  and either the water or the gas, respectively, is isotopically labeled. Differences between the two cases are evident despite the variability; profiles for case IV extend much deeper than case II and exhibit deeper and wider valleys near the surface. This latter behavior seems quite counterintuitive, as greater  $^{18}O$  enrichment in the gas and no enrichment in the liquid enhances the degree of fractionation.

Fig. 1c illustrates five metrics that were used to quantify the profiles:

- $F_{18}$ : net  $^{18}O_i$  injection flux.
- $C_{\min}$ : near-surface minimum of the  $^{18}O$  concentration in the “valley.”
- $W$ : width of the region for which the  $^{18}O$  concentration is below its natural abundance.
- $\lambda_1$  and  $\lambda_2$ : characteristic lengths describing bi-exponential decay, with  $\lambda_1 \ll \lambda_2$ .

$W$  and  $C_{\min}$  characterize the extent of isotopic fractionation, while  $\lambda_1$  and  $\lambda_2$  describe the penetration of  $^{18}O$  into the solid. The ESI<sup>†</sup> details the fitting procedures employed to obtain these metrics.

As shown in Fig. S2 and Table S2 of the ESI,<sup>†</sup> the metrics change regardless of the applied potential’s value. The mechanism by which the applied potential bias operates remains unknown. One possibility is that the electrode system unintentionally removes a contaminant that would normally poison injection sites. Alternatively, a form of electrostatic electrochemistry<sup>71,72</sup> operates, wherein redox reactions occur on statically charged insulators. The static charge in published reports is usually created by mechanical rubbing,<sup>73,74</sup> and whether charge transfer involves ions or electrons is still debated. A third possibility is that an electric field enhances injection.

Knowledge of the mechanism is not important for the focus of this work, which seeks to demonstrate the importance of bulk and surface O interstitials in mediating the exchange of O atoms between  $TiO_2$  and the liquid. Bulk and surface interstitials are already known to serve this purpose for  $TiO_2$  in water without applied bias, both thermally<sup>37</sup> and with UV stimulation.<sup>70</sup> As the sections below will show, applying potential bias does not change this picture. Applying bias simply accentuates the profile metrics compared to water without bias, thereby making measurement easier. For example, applying potential bias increases the net injection fluxes by over an order of magnitude, which steepens the gradient for fractionation and greatly extends the penetration of interstitials up to roughly 10  $\mu m$  into the solid. Accordingly, the  $^{18}O$ -depleted region’s width increases from an average of 2.8 nm

to as high as 90 nm. Isotopic depletion increases from an average factor of 1.4 below natural abundance to as high as 3.

### 3.1 Statistical tests for isotope and $O_2$ concentration effects

Table 1 shows the mean and standard deviation for each of the five metrics ( $F_{18}$ ,  $W$ ,  $C_{\min}$ ,  $\lambda_1$ ,  $\lambda_2$ ) for the four ambient conditions studied. The results in Table 1 appear as bar graphs in Fig. 2. The variability among profiles induces large standard deviations for each metric. Hence, statistical tests were employed to determine whether changes in the experimental conditions between cases lead to a significant change in the mean. Such tests yield a probability (“ $p$ -value”) that quantifies the likelihood of the null hypothesis being true. The null hypothesis is that a difference in the mean between two cases arises from random chance.

Histograms of the metric distributions for the largest data set (case III) exhibit considerable deviations from normality even after logarithmic transformation (Fig. S3 and S4 in the ESI<sup>†</sup>). The classical “parametric” Student’s  $t$ -test for comparing means exhibits considerable robustness to deviations from a normal distribution.<sup>75,76</sup> Nevertheless, we also employed a common “non-parametric” Mann–Whitney  $U$ -test that does not presuppose normality. There is no reason to believe cases I–IV have differently shaped distributions.

In such situations, a non-parametric test compares medians<sup>77</sup> rather than means. However, this difference in data aggregation affects the statistical power of  $t$  and Mann–Whitney tests (*i.e.*, the likelihood of detecting a statistically significant effect). The values for most of the metrics in Table 1 vary over 1.5 to 2 orders of magnitude (*e.g.*, 0.6 to 94 nm for  $W$ ). The means typically exceed the medians by a factor of 1.3 to 1.6. Thus, closely spaced small values are weighted more heavily than widely spaced large ones in a statistical test that compares medians instead of means. This property decreases the vulnerability of Mann–Whitney tests to type I errors that reject the null hypothesis when it is true but increases their vulnerability to type II errors that fail to reject the null hypothesis when it is false.

Table 2 shows the  $p$ -values for each metric obtained from  $t$ -tests and Mann–Whitney  $U$ -tests for all pairwise permutations of ambient conditions. The comparison of cases II–IV has particular importance because no change occurs in the chemical composition of either gas (pure  $O_2$ ) or liquid. Only the isotopic composition changes. Both tests yield  $p < 0.02$  for all profile metrics. In other words, the likelihood is very high that changing only the  $^{18}O$  mole fractions in the gas and liquid (at constant partial pressure of  $O_2$ ) suffices to influence all aspects of the

Table 1 Means and standard deviations (in parentheses) of profile metrics

	Case I	Case II	Case III	Case IV
$F_{18}$ ( $cm^{-2} s^{-1}$ )	$1.6(1.0) \times 10^{11}$	$1.2(0.6) \times 10^{11}$	$3.0(2.9) \times 10^{11}$	$5.1(4.5) \times 10^{11}$
$W$ (nm)	$8.3(5.3)$	$6.1(3.0)$	$13.6(14.4)$	$27.5(16.1)$
$C_{\min}$ ( $cm^{-3}$ )	$7.5(1.8) \times 10^{19}$	$8.3(1.4) \times 10^{19}$	$8.3(2.0) \times 10^{19}$	$4.2(1.0) \times 10^{19}$
$C_{\text{nat}} - C_{\min}$ ( $cm^{-3}$ )	$5.4(1.8) \times 10^{19}$	$4.6(1.4) \times 10^{19}$	$4.6(2.0) \times 10^{19}$	$8.6(1.0) \times 10^{19}$
$\lambda_1$ (nm)	$21(14)$	$17(10)$	$45(45)$	$80(79)$
$\lambda_2$ (nm)	$390(270)$	$240(140)$	$420(350)$	$1160(850)$



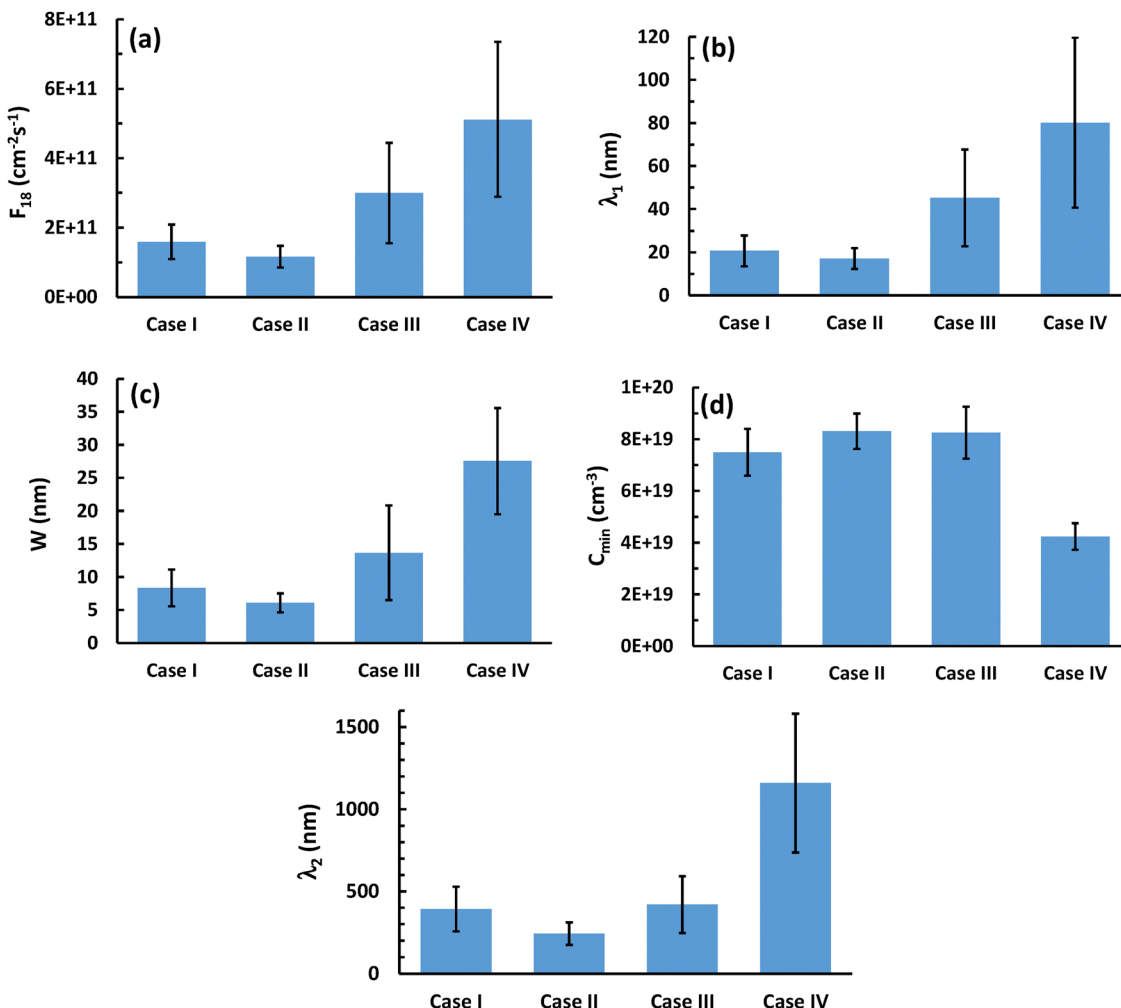


Fig. 2 Bar graphs showing means and standard deviations for profile metrics in each of the four cases: (a)  $F_{18}$  (b)  $\lambda_1$  (c)  $W$  (d)  $C_{\min}$  (e)  $\lambda_2$ . For all metrics, conditions are  $70^\circ\text{C}$ ,  $t = 60$  min.

Table 2 Pairwise statistical analyses of five metrics

Ambient pair	$F_{18}$ ( $\text{cm}^{-2} \text{s}^{-1}$ )		$C_{\min}$ ( $\text{cm}^{-3}$ )		$W$ (nm)		$\lambda_1$ (nm)		$\lambda_2$ (nm)	
	$p_{t\text{-test}}$	$p_{MW}$	$p_{t\text{-test}}$	$p_{MW}$	$p_{t\text{-test}}$	$p_{MW}$	$p_{t\text{-test}}$	$p_{MW}$	$p_{t\text{-test}}$	$p_{MW}$
Cases I-II	0.19	0.44	0.24	0.33	0.18	0.37	0.47	0.94	0.075	0.19
Cases I-III	$8 \times 10^{-4}$	0.15	0.12	0.45	0.018	0.20	$1 \times 10^{-4}$	0.038	0.73	0.83
Cases I-IV	0.022	$7 \times 10^{-4}$	$9 \times 10^{-7}$	$8 \times 10^{-5}$	$1 \times 10^{-3}$	$2 \times 10^{-4}$	0.027	$6 \times 10^{-4}$	0.010	$6 \times 10^{-4}$
Cases II-III	$4 \times 10^{-5}$	0.087	0.85	0.65	$4 \times 10^{-4}$	0.092	$4 \times 10^{-5}$	0.13	0.011	0.18
Cases II-IV	0.012	$8 \times 10^{-4}$	$1 \times 10^{-5}$	$2 \times 10^{-4}$	$4 \times 10^{-4}$	$4 \times 10^{-4}$	0.019	0.0014	0.0056	$5 \times 10^{-4}$
Cases III-IV	0.14	0.041	$1 \times 10^{-9}$	$4 \times 10^{-4}$	0.011	$1 \times 10^{-3}$	0.17	0.078	0.012	$7 \times 10^{-5}$

$^{18}\text{O}$  profiles. This result shows that  $\text{O}_2$  gas supplies some of the injected oxygen. Furthermore, the effects extend at least as deep as the largest individual value of  $\lambda_2$ , *i.e.*,  $>1 \mu\text{m}$ .

Cases I, II and III entail no change in isotopic composition of either gas or liquid; only the chemical concentration of  $\text{O}_2$  varies in the gas phase. The  $t$ -test  $p$ -values are rather large for I-II but are quite small for many metrics involving I-III and II-III. The corresponding Mann-Whitney  $p$ -values are noticeably larger for these latter two comparisons. However, the

$p$ -values for  $\lambda_1$  in I-III are quite small at 0.038 and are also rather small for  $F_{18}$  and  $W$  in II-III at 0.087 and 0.092, respectively. In combination, the two tests therefore agree that  $\text{O}_2$  concentration affects some metrics of the profiles.

### 3.2 DFT simulations

Fig. S5 (ESI†) shows surface geometries of both pristine and bridging hydroxylated  $\text{TiO}_2(110)$  surfaces. For the bridging hydroxylated surface, two hydrogen atoms occupy bridging



$O_{2f}$  sites to represent the fragments of liquid water dissociation. Fig. 3 displays the metastable surface geometries of O atoms adsorbed on pristine  $TiO_2(110)$ , which include dumbbell, split and on-top structures. The dumbbell and split configurations both associate two O atoms with a surface  $O_{3f}$  site originally occupied by a single O atom. The two atoms represent distorted versions of corresponding  $O_i$  configurations in the bulk reported previously, and thus act like ‘‘surface interstitials.’’<sup>57</sup> The structures remain minimally changed upon hydroxylation of the surface, as shown in Fig. 4. Table 3 summarizes the calculated adsorption energies and Bader charges in the limit of maximally O-rich conditions investigated here. Adsorption energies

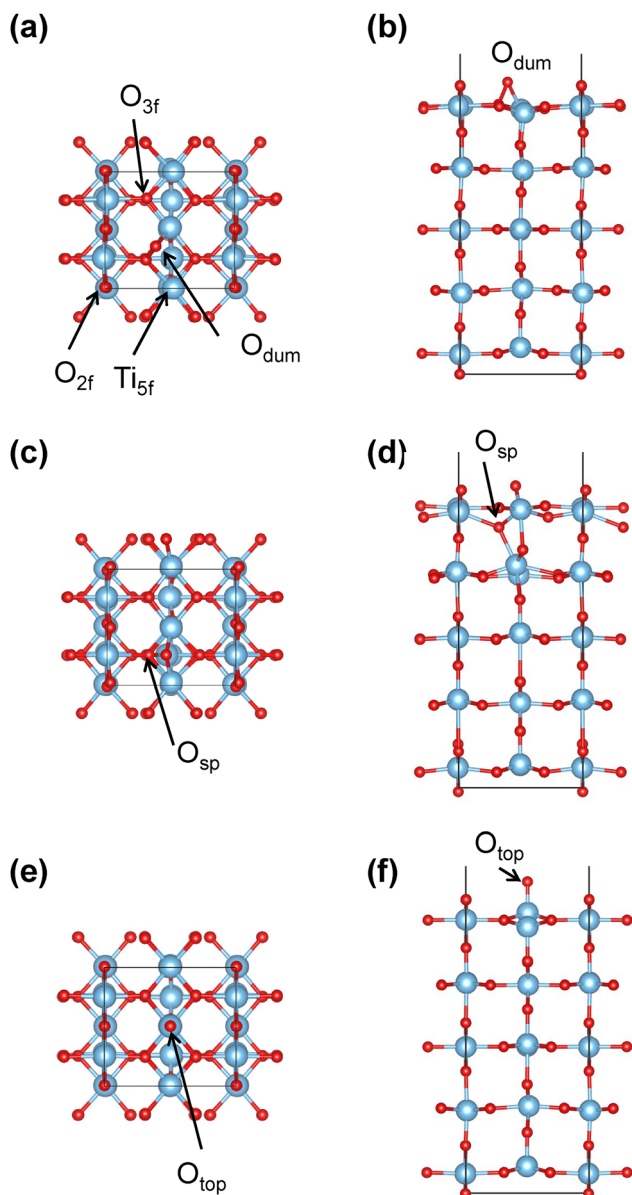


Fig. 3 Geometry of metastable adsorbed O configurations on pristine  $TiO_2(110)$  terraces, including (a) and (b) dumbbell ( $O_{dum}$ ), (c) and (d) split ( $O_{sp}$ ) and (e) and (f) on-top ( $O_{top}$ ). Panels (a), (c) and (e) show top views and (b), (d) and (f) show side views. Shading colors respectively represent blue for Ti and red for O.

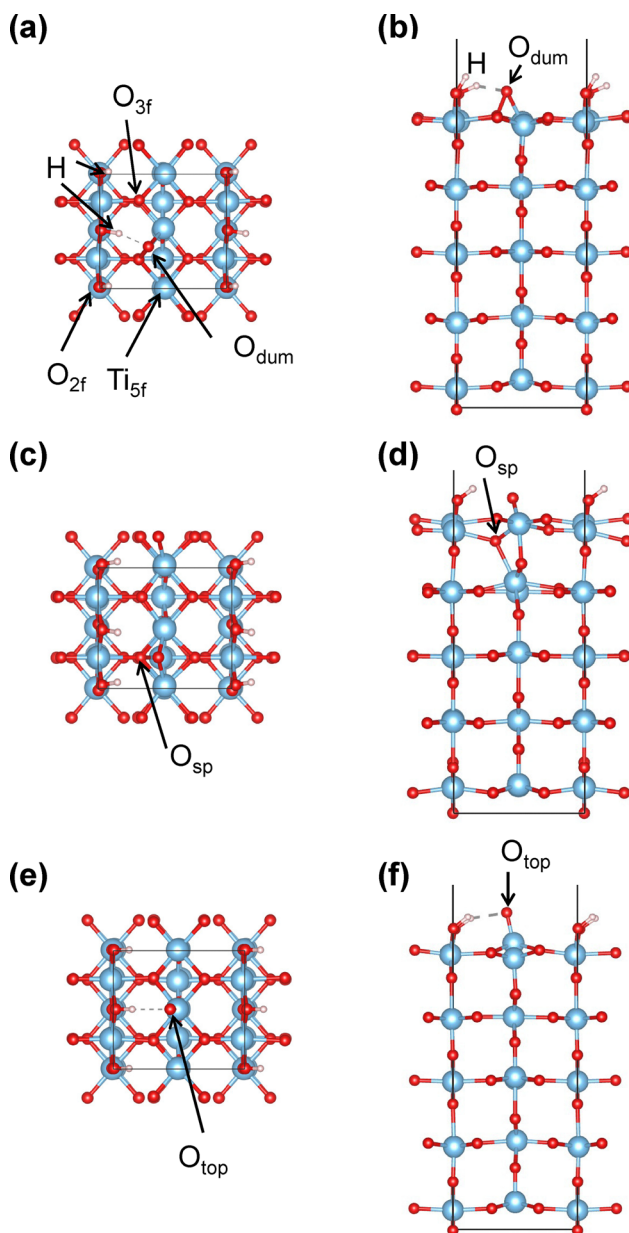


Fig. 4 Geometry of metastable adsorbed O configurations with co-adsorbed bridging hydroxyls on  $TiO_2(110)$  terraces, including (a) and (b) dumbbell ( $O_{dum}$ ), (c) and (d) split ( $O_{sp}$ ) and (e) and (f) on-top ( $O_{top}$ ). Panels (a), (c) and (e) show top views and (b), (d) and (f) show side views. Shading colors respectively represent blue for Ti and red for O, and white for H.

appear for values of  $E_F$  at the valence band maximum (VBM,  $E_F = 0$  eV) and conduction band minimum (CBM,  $E_F = 3.1$  eV). For completeness, Table S3 (ESI<sup>†</sup>) shows parallel results for maximally Ti-rich conditions.

Bader charge analysis of the dumbbell surface interstitial structure on the pristine surface shows  $-0.43e^-$  on the topmost atom and  $-0.69e^-$  on its nearest neighbor just below, for a sum of  $-1.12e^-$ . Previous analysis<sup>57</sup> has demonstrated this species to be neutral. By contrast, the split structure is known to be charged  $-2$ . The topmost atom has a Bader charge of  $-1.11e^-$ , and  $-0.94$  resides on the underlying nearest-neighbor O just

Table 3 Adsorption energy and Bader charge of adsorbed O on TiO<sub>2</sub>(110): O-rich conditions

TiO <sub>2</sub> (110) surface conditions	Adsorption configuration	Adsorption energy (eV)		Bader charge (e <sup>-</sup> )			Charge state
		$E_F = 0$ eV	$E_F = 3.1$ eV	Adsorbed O atom	Neighboring O atom	Charge state	
Pristine	Dumbbell	0.80	0.80	-0.43	-0.69	0	
	Split	0.95	-5.11	-1.11	-0.94	-2	
	On-top	2.63	-0.40	-0.61	-1.09	-1	
Bridging hydroxylated	Dumbbell	0.48	0.48	-0.54	-0.71	0	
	Split	-0.30	-6.36	-1.12	-1.03	-2	
	On-top	-2.21	-5.23	-0.87	-1.13	-1	

below for a total of  $-2.05e^-$ . For the on-top geometry, the adsorbed O has a Bader charge of  $-0.61e^-$ . The symmetry of this structure does not associate this O with any particular in-plane atom, but each of the four equivalent O<sub>3f</sub> nearest-neighbor atoms in the surface plane have a Bader charge of  $-1.09e^-$ . Thus, a sum comparable to those of the dumbbell and split configurations is  $-1.70e^-$ , which lies intermediate between the values for the dumbbell and the split. The calculations therefore suggest an on-top charge state of -1, consistent with previously published DFT results for isolated O.<sup>49</sup> For the hydroxylated surface, the Bader charges all become slightly more electron-rich, but the ordering does not change. Thus, we infer no change in charge state induced by hydroxylation.

For nearly all values of  $E_F$ , the adsorption energies on the pristine surface in Table 3 show that the split geometry is most stable (most negative). The dumbbell becomes most stable by a small margin when  $E_F$  is near the VBM. On the hydroxylated surface, the on-top geometry is most stable for  $E_F$  near the VBM, while the split is most stable for  $E_F$  near the CBM. In contrast with the surface interstitial structures, for the on-top configuration the adsorbed O atom pulls the underlying Ti atom significantly above the surface plane. Fig. 4e and f show that hydroxylation stabilizes the resulting bond stretching by pulling the adsorbed O laterally toward a nearby H atom. Much less stabilization is possible for the surface interstitial structures.

## 4. Discussion

### 4.1 Contributions of injected O from H<sub>2</sub>O and O<sub>2</sub>

The <sup>18</sup>O profiles provide strong evidence that both H<sub>2</sub>O and dissolved O<sub>2</sub> contribute O that diffuses into submerged TiO<sub>2</sub>. Do O<sub>2</sub> and H<sub>2</sub>O contribute independently or employ the same pathway? Adsorbate populations on submerged TiO<sub>2</sub> are dominated by OH (either anion or neutral) and molecular H<sub>2</sub>O.<sup>39–42</sup> Adsorbed OH is not very acidic,<sup>78</sup> yet experiments with deuterated water have shown<sup>37</sup> that oxygen injects as O<sub>i</sub>, not OH. Similar experiments performed here with applied bias yield the same results. This apparent paradox can be reconciled by the capacity for hydrogen bonding<sup>79</sup> and acid–base chemistry<sup>80</sup> afforded by the liquid phase. These solvation effects stabilize intermediates such as adsorbed O,<sup>35</sup> as evidenced by electron spin resonance<sup>81</sup> and photoluminescence.<sup>45</sup> Submersion can reduce the activation energy for O<sub>2</sub> dissociation<sup>82</sup> and increase the acidity of OH<sup>83</sup> by reducing the barrier for deprotonation.<sup>84</sup>

The temperature dependence of O<sub>i</sub> injection in submersion is much less than that of elementary-step injection of adsorbed O, which suggests the rate-limiting step is kinetically upstream.<sup>37</sup> Thus, there is ample reason to believe that deprotonation of OH to O limits the overall rate of O<sub>i</sub> creation, meaning that adsorbed OH serves as a single kinetic conduit for movement of O between the solid and fluid.

Note that solvation effects limit the mechanistic insights afforded by the large literature for *in vacuo* adsorption of H<sub>2</sub>O and O<sub>2</sub> on TiO<sub>2</sub>. As with submerged TiO<sub>2</sub>, those studies show that H<sub>2</sub>O can dissociate on TiO<sub>2</sub> and other common metal oxides. On TiO<sub>2</sub>, surface V<sub>O</sub> aids dissociation by providing adjacent cation and anion sites that bond readily to H<sub>2</sub>O and the products OH and H.<sup>40</sup> However, OH appears as the only oxygenated product<sup>39,61,85</sup> because no solvation is possible to stabilize adsorbed O. Without doping or photoexcitation, molecular O<sub>2</sub> chemisorption *in vacuo* requires electron donation from V<sub>O</sub> or other surface defects.<sup>40</sup> Dissociation of O<sub>2</sub> to O is favored by conditions that increase the electronegativity of the surface,<sup>40,86</sup> including the presence of electron donors such as surface V<sub>O</sub>.<sup>40,50</sup> However, gaseous O<sub>2</sub> does not adsorb and dissociate fast enough on TiO<sub>2</sub>(110) to inject O<sub>i</sub> unless temperatures exceed about 600 °C.<sup>87</sup> In submersion, solvation effects enable dissociation and injection of O<sub>i</sub> even at 70 °C.

The aftereffects of ion sputtering for surface cleaning also limit the direct translation of *in vacuo* mechanistic findings to TiO<sub>2</sub> submersion. Sputtering preferentially removes O from the solid, which chemically reduces some of the Ti and forms V<sub>O</sub>.<sup>40</sup> Reduction of the surface layer is irreversible *in vacuo* below 400 K<sup>40,88</sup> unless the ion fluence is low.<sup>40,89,90</sup> With low fluence, submersion quickly removes surface V<sub>O</sub> with dissolved O<sub>2</sub><sup>40,91,92</sup> or H<sub>2</sub>O itself.<sup>93–95</sup> However, submersion reverses V<sub>O</sub> formation in the near subsurface (2–3 nm) slowly and only partially.<sup>96</sup> This failure to reverse subsurface reduction reflects the suppression of Ti interstitials, which are central to *in vacuo* reversal of chemical reduction above 400 K.<sup>88</sup> Ti interstitials play no role at submersion temperatures because there is no generation mechanism, and their high mobility ensures their sequestration in bulk traps or at the surface.<sup>97</sup>

Two mathematical models were formulated and compared to test the hypothesis that OH serves as a single kinetic conduit for O. Model derivations appear in the ESI.† One model is agnostic about the injection mechanism (thereby not aligning with the hypothesis) and assumes that H<sub>2</sub>O and O<sub>2</sub> contribute O<sub>i</sub> and isotopic labels in linear proportion to their respective



total concentrations in the fluid. The net injection flux  $F_{18}$  of  $^{18}\text{O}$  (time-averaged) is then given by:

$$F_{18} = Y_{18,\text{W}}x F_{\text{W}} + Y_{18,\text{O}_2} X_{\text{O}_2} (1 - x) F_{\text{W}}, \quad (1)$$

where  $Y_{18,\text{W}}$  and  $Y_{18,\text{O}_2}$  respectively denote the mole fraction of  $^{18}\text{O}$  in water and  $\text{O}_2$ ,  $X_{\text{O}_2}$  denotes the chemical mole fraction of  $\text{O}_2$  (all isotopes) in the gas,  $x$  denotes the fraction of injected O originating from  $\text{H}_2\text{O}$ , and  $F_{\text{W}}$  is the net injection flux of O if only water supplies the oxygen.

The second model aligns with the hypothesis by presupposing a Langmuir-style dual pathway mechanism wherein both  $\text{O}_2$  and  $\text{H}_2\text{O}$  inject through the same adsorbed OH intermediate whose surface coverage does not vary. This differs slightly from "competitive adsorption," wherein  $\text{O}_2$  and  $\text{H}_2\text{O}$  compete for the same surface sites but have different coverages. For simplicity, first order kinetics are assumed for dissociative adsorption and desorption of  $\text{H}_2\text{O}$  and  $\text{O}_2$  to form adsorbed O. First order kinetics are also assumed for conversion of OH to injected O. The rate constant  $k_{\text{inj}}$  for injection is a composite quantity that implicitly contains the rate constants for deprotonation of OH and injection of O, and the concentration of adsorbed O. The resulting expression for  $F_{18}$  is:

$$F_{18} = k_{\text{inj}} \theta_{\text{OH},18} = k_{\text{inj}} \left[ \frac{Y_{18,\text{W}}x + Y_{18,\text{O}_2} X_{\text{O}_2} (1 - x)}{x + X_{\text{O}_2} (1 - x)} \right]. \quad (2)$$

In the asymptotic limit of  $x = 1$ , eqn (1) from the linear proportion model represents a limiting case of eqn (2) from the dual pathway model with  $F_{\text{W}} = k_{\text{inj}}$ . The dual pathway model has the same number of fitting parameters (two) as the linear proportion model but allows for possible "saturation" of adsorbed OH with gas-derived O as the  $\text{O}_2$  concentration rises. Thus, fitting eqn (1) and (2) to the means values from experiments offers a direct comparison with the same number of fitting parameters of two different models: one that allows for saturation and one that does not.

Linear regression using the linear proportion model yields  $x = 0.78$ ,  $F_{\text{W}} = 2.5 \times 10^{12} \text{ cm}^{-2} \text{ s}^{-1}$ , and a total residual variance of  $1.9 \times 10^{22} \text{ cm}^{-4} \text{ s}^{-2}$ . Nonlinear regression using the dual pathway model yields  $x = 0.76$ ,  $k_{\text{inj}} = 2.2 \times 10^{12} \text{ cm}^{-2} \text{ s}^{-1}$ , and a total residual variance of  $1.5 \times 10^{22} \text{ cm}^{-4} \text{ s}^{-2}$ . The factor of  $10^{22}$  in the variances can be removed by choosing different units or scaling. The point of comparison centers on the multiplying factors 1.5 vs. 1.9. The difference is modest, but the lower residual fitting error for the dual pathway model is consistent with the hypothesis that adsorbed OH provides the single conduit by which O exchanges between fluid and solid.

The two models yield nearly identical values for  $x$ . This factor almost certainly varies with temperature, pH and other experimental variables. Although  $\text{H}_2\text{O}$  provides most of the injected O in the present experiments,  $\text{O}_2$  also contributes significantly. Notably, the concentration of dissolved  $\text{O}_2$  at 70 °C is only  $0.83 \times 10^{-3}$  mole  $\text{l}^{-1}$ , while the concentration of  $\text{H}_2\text{O}$  is  $6.5 \times 10^4$  times higher at 54.2 mole  $\text{l}^{-1}$ . Therefore, the reaction rate constant to form injectable O via adsorbed OH must be considerably lower for  $\text{H}_2\text{O}$  than for  $\text{O}_2$ , which is

consistent with chemical intuition that  $\text{H}_2\text{O}$  is much less reactive than  $\text{O}_2$ .

## 4.2 Role of bulk O<sub>i</sub> in lattice O participation

As discussed elsewhere,<sup>37</sup> the diffusive penetration of  $^{18}\text{O}$  to hundreds of nanometers at 70 °C is very strong evidence that the diffusing species is O<sub>i</sub>. At this temperature, V<sub>O</sub> does not diffuse quickly enough to penetrate that far. The dominance of O<sub>i</sub> implies that V<sub>O</sub> has been eliminated by O<sub>i</sub> annihilation, both at the surface and within the bulk.<sup>37</sup>

The prevalence of O<sub>i</sub> to depths of hundreds of nanometers indicates that lattice O from these depths exchanges with O from both  $\text{H}_2\text{O}$  and dissolved O<sub>2</sub>. This can be seen as follows. In TiO<sub>2</sub>,<sup>67,87,98</sup> O<sub>i</sub> comprises two atoms symmetrically arranged around a single O lattice site. The atoms assume either a neutral "dumbbell" geometry with an O–O bond, or a charged "split" geometry with bonds only to surrounding metal cations. Diffusion of O<sub>i</sub> occurs by an interstitial mechanism, in which each constituent atom has a 50% chance of hopping – leaving its partner behind in the lattice. Although the net flow of O<sub>i</sub> is toward the deep bulk, numerous random hopping and lattice exchange events enable some O atoms from the deep bulk to reach the surface for transfer to the fluid.

Several factors drive O<sub>i</sub> creation at the surface. Some driving forces are energetic, impelled by defect reactions. An example is annihilation of V<sub>O</sub> by O<sub>i</sub>, which oxidizes the solid. Other examples include addition of O<sub>i</sub> to extended defects<sup>99</sup> and combination with adventitious hydrogen to form O<sub>i</sub>–H<sub>i</sub><sup>–</sup> (ref. 37) or other small clusters.<sup>57</sup> Another driving force is entropic. At 70 °C, the solid initially contains virtually no O<sub>i</sub> because this species has sufficient mobility to disappear at trap sites or the surface. The fluid maintains a continuous supply of adsorbed O, which converts into O<sub>i</sub> with a modest barrier near 0.8 eV<sup>29</sup> and spreads entropically into the solid.

The rate of O<sub>i</sub> generation observed here may be compared to the rate of a typical reaction involving O<sub>2</sub> on TiO<sub>2</sub> – the OER in photostimulated water splitting, which several groups have investigated on electrically conductive rutile TiO<sub>2</sub>(110).<sup>45,100–103</sup> Photocurrents range from 0.54 to 2.2 mA·cm<sup>–2</sup> under UV irradiation in the range from 0.2 to 7 mW·cm<sup>–2</sup>. These photocurrents correspond to O<sub>2</sub> molecular fluxes in the range 1–3 × 10<sup>15</sup> cm<sup>–2</sup> s<sup>–1</sup>. Here, F<sub>W</sub> or k<sub>inj</sub> set the rough magnitude of the O<sub>i</sub> injection fluxes – roughly three orders of magnitude lower. None of the photocurrent studies estimated their current efficiency, so competing reactions could have contributed to the measured current. However, O<sub>i</sub> injection seems to constitute only a minor side reaction.

## 4.3 Role of a "surface interstitial" in lattice O participation

Adsorbed O on TiO<sub>2</sub>(110) is usually depicted as sitting directly atop an underlying Ti<sub>5c</sub> atom based on *in vacuo* scanning probe experiments<sup>49–55</sup> and first principles simulations<sup>49,50,52–55</sup> including in submersion.<sup>46,56</sup> The charge state can be toggled between –1 and –2 with a scanning probe tip,<sup>53–55</sup> and this species has been represented in DFT simulations as both –1<sup>56</sup> and –2.<sup>46</sup> The present DFT calculations make plausible the hypothesis that both on-top and surface interstitial



(neutral dumbbell and charged split) configurations are metastable. The dominant form depends upon the value of  $E_F$ , the presence of liquid water, the energy barriers for interconversion, and other factors.

The on-top configuration is readily protonated. Protonation of the surface interstitial was not investigated here, but its high bond coordination implies little propensity for this reaction. Under some conditions the on-top and surface interstitial forms could coexist in comparable concentrations. Thus, there is good reason to believe that O moves from the fluid into the solid by a pathway in which  $H_2O$  or  $O_2$  form OH. O atoms produced by  $O_2$  dissociation convert rapidly to OH before injecting; in other words, equilibrium between OH and O greatly favors OH. However, that equilibrium involves the on-top form of O. Some of that form converts into the surface interstitial, which then injects as  $O_i$ . Diffusion of  $O_i$  into the solid ensues, followed by exchange into the lattice. Movement of O from the lattice into the fluid occurs through the reverse of these steps as depicted in Fig. 5.

This mechanistic picture can only be considered plausible, not proven. The present calculations simulate neither free water molecules nor the possibilities for hydrogen bonding

and protonation. Water molecules in the liquid probably screen hydrogen bonding interactions across rows, which seem especially effective at stabilizing the on-top structure. Moreover, liquid water changes relative stability in other ways, such as affecting the value of  $E_F$  at the surface *via* pH or dissolved ions that adsorb.

The foregoing discussion highlights a conceptual disconnect between computational simulations of adsorbed O focused on catalysis, photocatalysis and electrochemistry *vs.* those focused on defect reaction and diffusion in the solid. The former simulations typically emphasize mechanisms involving  $V_O$ , with little explicit consideration of  $E_F$  in the solid. The latter simulations emphasize  $O_i$  but treat liquid solvation and pH simplistically if at all. Both approaches yield useful insights, but further progress must account for contributions to the surface thermodynamics and kinetics from both the liquid and solid.

#### 4.4 Surface sites active for $O_i$ production

What kinds of surface sites other than  $V_O$  promote dissociation of  $H_2O$  and  $O_2$  in submersion? Clues come from fully amorphous metal oxides, which enhance activity for the OER through a wide variety of surface site geometries and their structural flexibility. Such sites are unfortunately difficult to characterize,<sup>104</sup> which is scientifically unsatisfying.<sup>61</sup> However, the design of “high-entropy” oxides embraces such complexity by adding five or more dopant metals to tune the behavior of active sites.<sup>23</sup> With rms surface roughness of  $0.14 \pm 0.08$  nm, the etched  $TiO_2$  employed here also supports ill-defined sites having a wide range of effectiveness for injecting  $O_i$ .<sup>58</sup>

What accounts for the susceptibility of  $TiO_2$  to poisoning of  $O_i$  creation? The most reactive sites on catalytic surfaces are often most vulnerable to deactivation by poisoning.<sup>105</sup> An example afflicts  $TiO_2$  photocatalysts used for the ORR to degrade aqueous pollutants,<sup>8,106,107</sup> wherein the poisons derive from dissolved organic matter. Deprotonation of OH and subsequent injection of  $O_i$  entails a form of heterogeneous catalysis, and a similar correlation between injection activity and poisoning susceptibility appears to hold for injection of  $O_i$  from oxide surfaces.<sup>58</sup>

#### 4.5 Implications for other oxides and reaction conditions

Because rutile  $TiO_2$  is a prototypical metal oxide, this picture based on  $O_i$  probably generalizes in many cases to other oxides – explaining important aspects of their thermal, electrochemical, and photochemical reactions with dissolved  $O_2$ . Examples include oxides fabricated to be hyperstoichiometric, including spinel ferrites,<sup>108–111</sup> perovskites,<sup>112</sup> and Ruddlesden–Popper oxides.<sup>29,30,113–115</sup> Hyperstoichiometric oxides permanently contain mobile  $O_i$ , and often exhibit enhanced catalysis and photocatalysis rates.<sup>29,30</sup>

In stoichiometric oxides,  $O_i$  adopts dumbbell or split configurations like those within  $TiO_2$  in wurtzite  $ZnO$ ,<sup>116–121</sup> corundum  $Al_2O_3$ ,<sup>122–124</sup> fluorite  $CaO$ ,<sup>125</sup> corundum  $Cr_2O_3$ ,<sup>126</sup> hematite  $Fe_2O_3$ ,<sup>127,128</sup> perovskite  $SrTiO_3$ ,<sup>129–131</sup> fluorite  $ThO_2$ ,<sup>125,132</sup> fluorite  $UO_2$ ,<sup>133,134</sup> tetragonal<sup>135</sup> and cubic  $ZrO_2$ ,<sup>136,137</sup> and

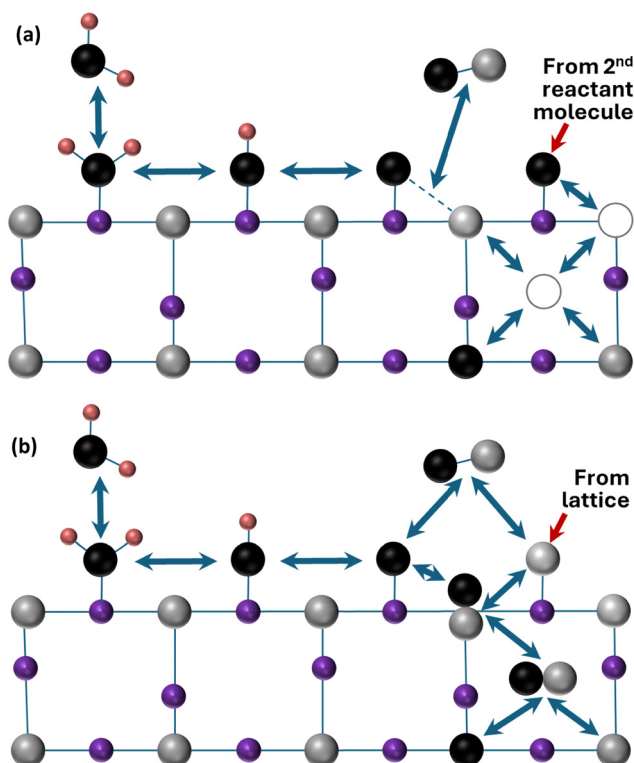


Fig. 5 Schematic comparison of O atom exchange between rutile  $TiO_2(110)$  and  $H_2O$  or dissolved  $O_2$  in the fluid – mediated by (a) O vacancies in the conventional picture and (b) O interstitials in the proposed picture. Diagrams do not attempt to represent exact geometric configurations or certain details of reaction stoichiometry, e.g., the fate of H or exchange of O between mobile species and the lattice. Balls depict atoms of Ti (purple) H (pink) and O originating primarily from the fluid (black) or solid lattice (grey). In reality, atoms originating from the fluid and solid are represented to some degree in all reaction and diffusion pathways.



Ruddlesden–Popper oxides.<sup>138</sup> Following the behavior of  $\text{TiO}_2$ , the formation energy for  $\text{O}_i$  in these oxides is typically lower than for  $\text{V}_\text{O}$  in O-rich environments,<sup>87,117,130,139,140</sup> as is the  $\text{O}_i$  hopping barrier.<sup>37,141</sup> To existing barrier compilations, low barriers for  $\text{O}_i$  hopping (0.13–0.47 eV) may be added for corundum  $\text{Cr}_2\text{O}_3$ ,<sup>126</sup> hematite  $\text{Fe}_2\text{O}_3$ ,<sup>128</sup> perovskite  $\text{SrTiO}_3$ ,<sup>129</sup> fluorite  $\text{ThO}_2$ ,<sup>125</sup> and fluorite  $\text{UO}_2$ .<sup>142</sup>

Counterintuitively,  $\text{O}_i$  may mediate aqueous reactions of O even in reduced oxides. The high diffusional mobility of  $\text{O}_i$  would make its dominance temporary and difficult to detect. Thus,  $\text{O}_i$  may dominate near the surface of vacancy-rich perovskites during reaction and then be replaced by  $\text{V}_\text{O}$  from the bulk after the reaction ends. Such behavior would accord with the malleability and rapid reversibility of perovskite surface composition and structure observed in other contexts.<sup>32</sup>

## 5. Conclusions

Isotopic self-diffusion measurements in submerged rutile  $\text{TiO}_2$  single crystals with varying concentrations of  $^{18}\text{O}$  isotopic label show that O exchange occurs between rutile  $\text{TiO}_2(110)$  and dissolved  $\text{O}_2$  as well as the  $\text{H}_2\text{O}$  liquid. Diffusion in the  $\text{TiO}_2$  is mediated by oxygen interstitials ( $\text{O}_i$ ). First-principles calculations strongly suggest that adsorbed O in on-top and “surface interstitial” configurations mediate the surface reaction rather than  $\text{V}_\text{O}$ . Adsorbed OH appears to provide a single pathway for  $\text{H}_2\text{O}$  and  $\text{O}_2$  to contribute injectable oxygen, although fitting the diffusion data to simple models indicates that  $\text{H}_2\text{O}$  contributes more. The most active sites on the surface for OH deprotonation and  $\text{O}_i$  injection are probably ill-defined and vulnerable to deactivation by poisoning. Compared to the rate of a typical reaction between  $\text{O}_2$  and  $\text{TiO}_2$  such as photostimulated OER, the rate of  $\text{O}_i$  injection is small. Because rutile  $\text{TiO}_2$  is a prototypical metal oxide, this physical picture helps to explain many aspects of thermal, electrochemical, and photochemical reactions between dissolved  $\text{O}_2$  and a variety of oxides.

## Data availability

The data that support the findings of this study are included within the article and its ESI.†

## Conflicts of interest

There are no conflicts to declare.

## Acknowledgements

This work was supported by the U.S. National Science Foundation under grant DMR 17-09327 and DMR 23-22121, and the Air Force Office of Scientific Research under grant FA9550-21-0078. SIMS and XPS measurements were performed in the Materials Research Laboratory Central Research Facilities, University of Illinois at Urbana-Champaign. We gratefully acknowledge the

use of high-performance computing (HPC) resources, such as Nurion and Neuron, provided by the R&D Innovation-Support Program at the Korea Institute of Science and Technology Information (KISTI). We are grateful to Dr. Stephen D. Bond for helpful advice on curve-fitting the  $^{18}\text{O}$  profiles.

## References

- 1 M. Rafique, S. Hajra, M. Irshad, M. Usman, M. Imran, M. A. Assiri and W. M. Ashraf, Hydrogen Production Using  $\text{TiO}_2$ -Based Photocatalysts: A Comprehensive Review, *ACS Omega*, 2023, **8**, 25640–25648.
- 2 Y. Nosaka, Water Photo-Oxidation over  $\text{TiO}_2$ —History and Reaction Mechanism, *Catalysts*, 2022, **12**, 1557.
- 3 H. Eidsvåg, S. Bentouba, P. Vajeeston, S. Yohi and D. Velauthapillai,  $\text{TiO}_2$  as a Photocatalyst for Water Splitting—An Experimental and Theoretical Review, *Molecules*, 2021, **26**, 1687.
- 4 A. Miyoshi, S. Nishioka and K. Maeda, Water Splitting on Rutile  $\text{TiO}_2$ -Based Photocatalysts, *Chem. – Eur. J.*, 2018, **24**, 18204–18219.
- 5 S. Chen and Y. H. Hu, Color  $\text{TiO}_2$  Materials as Emerging Catalysts for Visible-NIR Light Photocatalysis, A Review, *Catal. Rev.*, 2024, **66**, 1951–1991.
- 6 M. A. Al-Nuaim, A. A. Alwasiti and Z. Y. Shnain, The photocatalytic process in the treatment of polluted water, *Chem. Pap.*, 2023, **77**, 677–701.
- 7 H. Wang, X. Li, X. Zhao, C. Li, X. Song, P. Zhang, P. Huo and X. Li, A review on heterogeneous photocatalysis for environmental remediation: From semiconductors to modification strategies, *Chin. J. Catal.*, 2022, **43**, 178–214.
- 8 L. Ren, W. Huo, G. Li, W. Choi and T. An, Photocatalytic mechanisms and photocatalyst deactivation during the degradation of 5-fluorouracil in water, *Catal. Today*, 2023, **410**, 45–55.
- 9 G. Ren, H. Han, Y. Wang, S. Liu, J. Zhao, X. Meng and Z. Li, Recent Advances of Photocatalytic Application in Water Treatment: A Review, *Nanomaterials*, 2021, **11**, 1804.
- 10 H. Sheng, H. Ji, W. Ma, C. Chen and J. Zhao, Direct Four-Electron Reduction of  $\text{O}_2$  to  $\text{H}_2\text{O}$  on  $\text{TiO}_2$  Surfaces by Pendant Proton Relay, *Angew. Chem., Int. Ed.*, 2013, **52**, 9686–9690.
- 11 H. Du, H. Luo, M. Jiang, X. Yan, F. Jiang and H. Chen, A review of activating lattice oxygen of metal oxides for catalytic reactions: Reaction mechanisms, modulation strategies of activity and their practical applications, *Appl. Catal., A*, 2023, **664**, 119348.
- 12 J. Chen, W. Zhang, H. Li, W. Li and D. Zhao, Recent advances in  $\text{TiO}_2$ -based catalysts for  $\text{N}_2$  reduction reaction, *SusMat*, 2021, **1**, 174–193.
- 13 X.-Y. Xie, P. Xiao, W.-H. Fang, G. Cui and W. Thiel, Probing Photocatalytic Nitrogen Reduction to Ammonia with Water on the Rutile  $\text{TiO}_2(110)$  Surface by First-Principles Calculations, *ACS Catal.*, 2019, **9**, 9178–9187.



14 E. Tayyebi, Á. B. Höskuldsson, A. Wark, N. Atrak, B. M. Comer, A. J. Medford and E. Skúlason, Perspectives on the Competition between the Electrochemical Water and N<sub>2</sub> Oxidation on a TiO<sub>2</sub>(110) Electrode, *J. Phys. Chem. Lett.*, 2022, **13**, 6123–6129.

15 H. Hirakawa, M. Hashimoto, Y. Shiraishi and T. Hirai, Photocatalytic Conversion of Nitrogen to Ammonia with Water on Surface Oxygen Vacancies of Titanium Dioxide, *J. Am. Chem. Soc.*, 2017, **139**, 10929–10936.

16 P.-W. Huang and M. C. Hatzell, Prospects and good experimental practices for photocatalytic ammonia synthesis, *Nat. Commun.*, 2022, **13**, 7908.

17 R. B. Domínguez-Espíndola, D. M. Arias, C. Rodríguez-González and P. J. Sebastian, A critical review on advances in TiO<sub>2</sub>-based photocatalytic systems for CO<sub>2</sub> reduction, *Appl. Therm. Eng.*, 2022, **216**, 119009.

18 J. Chen, T. Li, X. An and D. Fu, Photocatalytic Reduction of CO<sub>2</sub> by TiO<sub>2</sub> Modified Materials: Recent Advances and Outlook, *Energy Fuels*, 2024, **38**, 7614–7636.

19 Z. Chen, H. Chen, K. Wang, J. Chen, M. Li, Y. Wang, P. Tsiaikaras and S. Song, Enhanced TiO<sub>2</sub> Photocatalytic 2 e – Oxygen Reduction Reaction *via* Interfacial Micro-environment Regulation and Mechanism Analysis, *ACS Catal.*, 2023, **13**, 6497–6508.

20 B. Bastug Azer, A. Gulsaran, J. R. Pennings, R. Saritas, S. Kocer, J. L. Bennett, Y. Devdas Abhang, M. A. Pope, E. Abdel-Rahman and M. Yavuz, A Review: TiO<sub>2</sub> based photoelectrocatalytic chemical oxygen demand sensors and their usage in industrial applications, *J. Electroanal. Chem.*, 2022, **918**, 116466.

21 Y.-F. Li and A. Selloni, Pathway of Photocatalytic Oxygen Evolution on Aqueous TiO<sub>2</sub> Anatase and Insights into the Different Activities of Anatase and Rutile, *ACS Catal.*, 2016, **6**, 4769–4774.

22 C. Zhao, H. Tian, Z. Zou, H. Xu and S.-Y. Tong, Understanding oxygen evolution mechanisms by tracking charge flow at the atomic level, *iScience*, 2023, **26**, 107037.

23 S. C. Pathan, J. S. Shaikh, M. Rittiruam, T. Saelee, V. Márquez, P. Khajondetchairit, S. S. Mali, J. V. Patil, C. K. Hong, P. Praserthdam and S. Praserthdam, High entropy metal oxide/TiO<sub>2</sub> nanocomposite for electrocatalytic overall water splitting, *J. Alloys Compd.*, 2024, 176811.

24 A. Grimaud, O. Diaz-Morales, B. Han, W. T. Hong, Y.-L. Lee, L. Giordano, K. A. Stoerzinger, M. T. M. Koper and Y. Shao-Horn, Activating lattice oxygen redox reactions in metal oxides to catalyse oxygen evolution, *Nat. Chem.*, 2017, **9**, 457–465.

25 J. T. Mefford, X. Rong, A. M. Abakumov, W. G. Hardin, S. Dai, A. M. Kolpak, K. P. Johnston and K. J. Stevenson, Water electrolysis on La<sub>1-x</sub>Sr<sub>x</sub>CoO<sub>3-δ</sub> perovskite electrocatalysts, *Nat. Commun.*, 2016, **7**, 11053.

26 J. S. Yoo, Y. Liu, X. Rong and A. M. Kolpak, Electronic Origin and Kinetic Feasibility of the Lattice Oxygen Participation During the Oxygen Evolution Reaction on Perovskites, *J. Phys. Chem. Lett.*, 2018, **9**, 1473–1479.

27 A. M. Frandsen, K. M. Macounová, J. Rossmeisl and P. Krtík, Lattice oxygen evolution in rutile Ru<sub>1-x</sub>Ni<sub>x</sub>O<sub>2</sub> electrocatalysts, *Electrochim. Acta*, 2024, **497**, 144567.

28 X. Tan, M. Zhang, D. Chen, W. Li, W. Gou, Y. Qu and Y. Ma, Electrochemical Etching Switches Electrocatalytic Oxygen Evolution Pathway of IrO<sub>x</sub>/Y<sub>2</sub>O<sub>3</sub> from Adsorbate Evolution Mechanism to Lattice-Oxygen-Mediated Mechanism, *Small*, 2023, **19**, 2303249.

29 B. Yin, Y. Li, N. Sun, X. Ji, Y. Huan, D. Dong, X. Hu and T. Wei, Activating ORR and OER in Ruddlesden–Popper based catalysts by enhancing interstitial oxygen and lattice oxygen redox reactions, *Electrochim. Acta*, 2021, **370**, 137747.

30 Y. Huan, S. Chen, R. Zeng, T. Wei, D. Dong, X. Hu and Y. Huang, Intrinsic Effects of Ruddlesden–Popper-Based Bifunctional Catalysts for High-Temperature Oxygen Reduction and Evolution, *Adv. Energy Mater.*, 2019, **9**, 1901573.

31 S. Ding, Y. Zhang, F. Lou, M. Li, Q. Huang, K. Yang, B. Xia, C. Tang, J. Duan, M. Antonietti and S. Chen, Oxygen-vacancy-type Mars–van Krevelen mechanism drives ultra-fast dioxygen electroreduction to hydrogen peroxide, *Mater. Today Energy*, 2023, **38**, 101430.

32 J. Song, C. Wei, Z.-F. Huang, C. Liu, L. Zeng, X. Wang and Z. J. Xu, A review on fundamentals for designing oxygen evolution electrocatalysts, *Chem. Soc. Rev.*, 2020, **49**, 2196–2214.

33 Y. Yang, K. Xu and X. Ma, Catalytic Mechanism of Oxygen Vacancy Defects in Metal Oxides, *Prog. Chem.*, 2023, **35**, 543–559.

34 J. Ferreira de Araújo, F. Dionigi, T. Merzdorf, H.-S. Oh and P. Strasser, Evidence of Mars–Van–Krevelen Mechanism in the Electrochemical Oxygen Evolution on Ni-Based Catalysts, *Angew. Chem., Int. Ed.*, 2021, **60**, 14981–14988.

35 T. E. Jones, D. Teschner and S. Piccinin, Toward Realistic Models of the Electrocatalytic Oxygen Evolution Reaction, *Chem. Rev.*, 2024, **124**, 9136–9223.

36 H. A. Tahini, X. Tan, U. Schwingenschlögl and S. C. Smith, Formation and Migration of Oxygen Vacancies in SrCoO<sub>3</sub> and Their Effect on Oxygen Evolution Reactions, *ACS Catal.*, 2016, **6**, 5565–5570.

37 H. Jeong, E. Ertekin and E. G. Seebauer, Surface-Based Post-synthesis Manipulation of Point Defects in Metal Oxides Using Liquid Water, *ACS Appl. Mater. Interfaces*, 2022, **14**, 34059–34068.

38 H. Jeong and E. G. Seebauer, Strong Isotopic Fractionation of Oxygen in TiO<sub>2</sub> Obtained by Surface-Enhanced Solid-State Diffusion, *J. Phys. Chem. Lett.*, 2022, **13**, 9841–9847.

39 U. Diebold, Perspective: A controversial benchmark system for water-oxide interfaces: H<sub>2</sub>O/TiO<sub>2</sub>(110), *J. Chem. Phys.*, 2017, **147**, 40901.

40 O. Berger, Understanding the fundamentals of TiO<sub>2</sub> surfacesPart II. Reactivity and surface chemistry of TiO<sub>2</sub> single crystals, *Surf. Eng.*, 2022, **38**, 846–906.

41 Z. Zeng, F. Wodaczek, K. Liu, F. Stein, J. Hutter, J. Chen and B. Cheng, Mechanistic insight on water dissociation on pristine low-index TiO<sub>2</sub> surfaces from machine learning molecular dynamics simulations, *Nat. Commun.*, 2023, **14**, 6131.



42 C. Di Valentin, A. Tilocca, A. Selloni, T. J. Beck, A. Klust, M. Batzill, Y. Losovjy and U. Diebold, Adsorption of Water on Reconstructed Rutile  $\text{TiO}_2(011)$ - $(2 \times 1)$ :  $\text{Ti}=\text{O}$  Double Bonds and Surface Reactivity, *J. Am. Chem. Soc.*, 2005, **127**, 9895–9903.

43 N. Siemer, D. Muñoz-Santiburcio and D. Marx, Solvation-Enhanced Oxygen Activation at Gold/Titania Nanocatalysts, *ACS Catal.*, 2020, **10**, 8530–8534.

44 F. Liu, N. Feng, Q. Wang, J. Xu, G. Qi, C. Wang and F. Deng, Transfer Channel of Photoinduced Holes on a  $\text{TiO}_2$  Surface As Revealed by Solid-State Nuclear Magnetic Resonance and Electron Spin Resonance Spectroscopy, *J. Am. Chem. Soc.*, 2017, **139**, 10020–10028.

45 A. Imanishi, T. Okamura, N. Ohashi, R. Nakamura and Y. Nakato, Mechanism of Water Photooxidation Reaction at Atomically Flat  $\text{TiO}_2$  (Rutile) (110) and (100) Surfaces: Dependence on Solution pH, *J. Am. Chem. Soc.*, 2007, **129**, 11569–11578.

46 Y.-B. Zhuang and J. Cheng, Deciphering the Anomalous Acidic Tendency of Terminal Water at Rutile(110)-Water Interfaces, *J. Phys. Chem. C*, 2023, **127**, 10532–10540.

47 P. Gono, F. Ambrosio and A. Pasquarello, Effect of the Solvent on the Oxygen Evolution Reaction at the  $\text{TiO}_2$ -Water Interface, *J. Phys. Chem. C*, 2019, **123**, 18467–18474.

48 L. J. Falling, J. J. Velasco-Vélez, R. V. Mom, A. Knop-Gericke, R. Schlögl, D. Teschner and T. E. Jones, The ladder towards understanding the oxygen evolution reaction, *Curr. Opin. Electrochem.*, 2021, **30**, 100842.

49 I. Sokolović, M. Reticcioli, M. Čalkovský, M. Wagner, M. Schmid, C. Franchini, U. Diebold and M. Setvín, Resolving the adsorption of molecular  $\text{O}_2$  on the rutile  $\text{TiO}_2(110)$  surface by noncontact atomic force microscopy, *Proc. Natl. Acad. Sci. U. S. A.*, 2020, **117**, 14827–14837.

50 E. Lira, J. Ø. Hansen, P. Huo, R. Bechstein, P. Galliker, E. Lægsgaard, B. Hammer, S. Wendt and F. Besenbacher, Dissociative and molecular oxygen chemisorption channels on reduced rutile  $\text{TiO}_2(110)$ : An STM and TPD study, *Surf. Sci.*, 2010, **604**, 1945–1960.

51 H. F. Wen, H. Sang, Y. Sugawara and Y. J. Li, Imaging oxygen molecular adsorption and dissociation on the Ti site of rutile  $\text{TiO}_2(110)$  surface with real configuration at 78 K by atomic force microscopy, *Phys. Chem. Chem. Phys.*, 2020, **22**, 19795–19801.

52 I. Lyubinetsky, N. A. Deskins, Y. Du, E. K. Vestergaard, D. J. Kim and M. Dupuis, Adsorption states and mobility of trimethylacetic acid molecules on reduced  $\text{TiO}_2(110)$  surface, *Phys. Chem. Chem. Phys.*, 2010, **12**, 5986–5992.

53 Q. Zhang, H. F. Wen, Y. Adachi, M. Miyazaki, Y. Sugawara, R. Xu, Z. H. Cheng and Y. J. Li, Electrical Engineering of the Oxygen Adatom and Vacancy on Rutile  $\text{TiO}_2(110)$  by Atomic Force Microscopy at 78 K, *J. Phys. Chem. C*, 2019, **123**, 28852–28858.

54 Q. Zhang, Y. J. Li, H. F. Wen, Y. Adachi, M. Miyazaki, Y. Sugawara, R. Xu, Z. H. Cheng, J. Brndiar, L. Kantorovich and I. Štich, Measurement and Manipulation of the Charge State of an Adsorbed Oxygen Adatom on the Rutile  $\text{TiO}_2(110)$ - $1 \times 1$  Surface by nc-AFM and KPFM, *J. Am. Chem. Soc.*, 2018, **140**, 15668–15674.

55 Y. Adachi, J. Brndiar, H. F. Wen, Q. Zhang, M. Miyazaki, S. Thakur, Y. Sugawara, H. Sang, Y. Li, I. Štich and L. Kantorovich, Electron dynamics of tip-tunable oxygen species on  $\text{TiO}_2$  surface, *Commun. Mater.*, 2021, **2**, 71.

56 D. Wang, T. Sheng, J. Chen, H.-F. Wang and P. Hu, Identifying the key obstacle in photocatalytic oxygen evolution on rutile  $\text{TiO}_2$ , *Nat. Catal.*, 2018, **1**, 291–299.

57 H. Jeong, E. G. Seebauer and E. Ertekin, Fermi level dependence of gas-solid oxygen defect exchange mechanism on  $\text{TiO}_2(110)$  by first-principles calculations, *J. Chem. Phys.*, 2020, **153**, 124710.

58 H. Jeong and E. G. Seebauer, Effects of adventitious impurity adsorption on oxygen interstitial injection rates from submerged  $\text{TiO}_2$  (110) and  $\text{ZnO}(0001)$  surfaces, *J. Vac. Sci. Technol. A*, 2023, **41**, 033203.

59 R. L. Kurtz, R. Stock-Bauer, T. E. Msdey, E. Román and J. L. De Segovia, Synchrotron radiation studies of  $\text{H}_2\text{O}$  adsorption on  $\text{TiO}_2(110)$ , *Surf. Sci.*, 1989, **218**, 178–200.

60 R. Wang, B. Wang, A. S. Abdullahi and H. Fan, Understanding the prototype catalyst  $\text{TiO}_2$  surface with the help of density functional theory calculation, *Wiley Interdiscip. Rev. Comput. Mol. Sci.*, 2024, **14**, e1686.

61 Z. Jakub, M. Meier, F. Kraushofer, J. Balajka, J. Pavělec, M. Schmid, C. Franchini, U. Diebold and G. S. Parkinson, Rapid oxygen exchange between hematite and water vapor, *Nat. Commun.*, 2021, **12**, 6488.

62 G. Kresse and J. Furthmüller, Efficient iterative schemes for ab initio total-energy calculations using a plane-wave basis set, *Phys. Rev. B: Condens. Matter Mater. Phys.*, 1996, **54**, 11169–11186.

63 G. Kresse and J. Furthmüller, Efficiency of ab-initio total energy calculations for metals and semiconductors using a plane-wave basis set, *Comput. Mater. Sci.*, 1996, **6**, 15–50.

64 A. Jain, S. P. Ong, G. Hautier, W. Chen, W. D. Richards, S. Dacek, S. Cholia, D. Gunter, D. Skinner, G. Ceder and K. A. Persson, Commentary: The Materials Project: A materials genome approach to accelerating materials innovation, *APL Mater.*, 2013, **1**, 011002.

65 J. P. Perdew, K. Burke and M. Ernzerhof, Generalized Gradient Approximation Made Simple, *Phys. Rev. Lett.*, 1996, **77**, 3865–3868.

66 G. Kresse and D. Joubert, From ultrasoft pseudopotentials to the projector augmented-wave method, *Phys. Rev. B: Condens. Matter Mater. Phys.*, 1999, **59**, 1758–1775.

67 H. Jeong, E. G. Seebauer and E. Ertekin, First-principles description of oxygen self-diffusion in rutile  $\text{TiO}_2$ : Assessment of uncertainties due to enthalpy and entropy contributions, *Phys. Chem. Chem. Phys.*, 2018, **20**, 17448–17457.

68 U. Aschauer and A. Selloni, Structure of the Rutile  $\text{TiO}_2(011)$  Surface in an Aqueous Environment, *Phys. Rev. Lett.*, 2011, **106**, 166102.

69 R. Krishna, Uphill diffusion in multicomponent mixtures, *Chem. Soc. Rev.*, 2015, **44**, 2812–2836.



70 H. Jeong and E. G. Seebauer, Effects of Ultraviolet Illumination on Oxygen Interstitial Injection from  $\text{TiO}_2$  under Liquid Water, *J. Phys. Chem. C*, 2022, **126**, 20800–20806.

71 J. Zhang, S. Ferrie, S. Zhang, Y. B. Vogel, C. R. Peiris, N. Darwish and S. Ciampi, Single-Electrode Electrochemistry: Chemically Engineering Surface Adhesion and Hardness To Maximize Redox Work Extracted from Tribocharged Silicon, *ACS Appl. Nano Mater.*, 2019, **2**, 7230–7236.

72 C. Liu and A. J. Bard, Electrons on dielectrics and contact electrification, *Chem. Phys. Lett.*, 2009, **480**, 145–156.

73 C. Liu and A. J. Bard, Chemical Redox Reactions Induced by Cryptoelectrons on a PMMA Surface, *J. Am. Chem. Soc.*, 2009, **131**, 6397–6401.

74 J. Zhang, F. J. M. Rogers, N. Darwish, V. R. Gonçales, Y. B. Vogel, F. Wang, J. J. Gooding, M. Chandramalika, R. Peiris, G. Jia, J.-P. Veder, M. L. Coote and S. Ciampi, Electrochemistry on Tribocharged Polymers Is Governed by the Stability of Surface Charges Rather than Charging Magnitude, *J. Am. Chem. Soc.*, 2019, **141**, 5863–5870.

75 M. J. Blanca, R. Alarcón, J. Arnau, R. Bono and R. Bendayan, Datos no normales: ¿es el ANOVA una opción válida?, *Psicothema*, 2017, **29**, 552–557.

76 M. M. Ali and S. C. Sharma, Robustness to nonnormality of regression F-tests, *J. Econom.*, 1996, **71**, 175–205.

77 M. P. Perme and D. Manevski, Confidence intervals for the Mann–Whitney test, *Stat. Methods Med. Res.*, 2018, **28**, 3755–3768.

78 R. L. Kurtz, R. Stock-Bauer, T. E. Msdey, E. Román and J. L. De Segovia, Synchrotron radiation studies of  $\text{H}_2\text{O}$  adsorption on  $\text{TiO}_2(110)$ , *Surf. Sci.*, 1989, **218**, 178–200.

79 H. Sheng, H. Zhang, W. Song, H. Ji, W. Ma, C. Chen and J. Zhao, Activation of Water in Titanium Dioxide Photocatalysis by Formation of Surface Hydrogen Bonds: An In Situ IR Spectroscopy Study, *Angew. Chem., Int. Ed.*, 2015, **54**, 5905–5909.

80 D. Rosa, G. Manetta and L. Di Palma, Experimental assessment of the pH effect and ions on the photocatalytic activity of iron-doped titanium dioxide supported on polystyrene pellets: Batch and continuous tests, *Chem. Eng. Sci.*, 2024, **291**, 119918.

81 F. Liu, N. Feng, Q. Wang, J. Xu, G. Qi, C. Wang and F. Deng, Transfer Channel of Photoinduced Holes on a  $\text{TiO}_2$  Surface As Revealed by Solid-State Nuclear Magnetic Resonance and Electron Spin Resonance Spectroscopy, *J. Am. Chem. Soc.*, 2017, **139**, 10020–10028.

82 N. Siemer, D. Muñoz-Santiburcio and D. Marx, Solvation-Enhanced Oxygen Activation at Gold/Titania Nanocatalysts, *ACS Catal.*, 2020, **10**, 8530–8534.

83 Y.-B. Zhuang and J. Cheng, Deciphering the Anomalous Acidic Tendency of Terminal Water at Rutile(110)–Water Interfaces, *J. Phys. Chem. C*, 2023, **127**, 10532–10540.

84 P. Gono, F. Ambrosio and A. Pasquarello, Effect of the Solvent on the Oxygen Evolution Reaction at the  $\text{TiO}_2$ –Water Interface, *J. Phys. Chem. C*, 2019, **123**, 18467–18474.

85 Y. Wang, M. Muhler and C. Wöll, Spectroscopic evidence for the partial dissociation of  $\text{H}_2\text{O}$  on  $\text{ZnO}(100)$ , *Phys. Chem. Chem. Phys.*, 2006, **8**, 1521–1524.

86 H. F. Wen, M. Miyazaki, Q. Zhang, Y. Adachi, Y. J. Li and Y. Sugawara, Direct observation of atomic step edges on the rutile  $\text{TiO}_2(110)$ –(1  $\times$  1) surface using atomic force microscopy, *Phys. Chem. Chem. Phys.*, 2018, **20**, 28331–28337.

87 H. Jeong, E. Ertekin and E. G. Seebauer, Kinetic Control of Oxygen Interstitial Interaction with  $\text{TiO}_2(110)$  via the Surface Fermi Energy, *Langmuir*, 2020, **36**, 12632–12648.

88 M. A. Henderson, A surface perspective on self-diffusion in rutile  $\text{TiO}_2$ , *Surf. Sci.*, 1999, **419**, 174–187.

89 F. Li, B. Wang, X. Chen, Y. Lai, T. Wang, H. Fan, X. Yang and Q. Guo, Photocatalytic Oxidative Dehydrogenation of Propane for Selective Propene Production with  $\text{TiO}_2$ , *JACS Au*, 2022, **2**, 2607–2616.

90 Y. Lai, R. Wang, Y. Zeng, F. Li, X. Chen, T. Wang, H. Fan and Q. Guo, Low-Temperature Oxidation of Methane on Rutile  $\text{TiO}_2(110)$ : Identifying the Role of Surface Oxygen Species, *JACS Au*, 2024, **4**, 1396–1404.

91 M. Al-Hashem, S. Akbar and P. Morris, Role of Oxygen Vacancies in Nanostructured Metal-Oxide Gas Sensors: A Review, *Sens. Actuators, B*, 2019, **301**, 126845.

92 N. G. Petrik, Z. Zhang, Y. Du, Z. Dohnálek, I. Lyubinetsky and G. A. Kimmel, Chemical Reactivity of Reduced  $\text{TiO}_2(110)$ : The Dominant Role of Surface Defects in Oxygen Chemisorption, *J. Phys. Chem. C*, 2009, **113**, 12407–12411.

93 O. Bikondoa, C. L. Pang, R. Ithnin, C. A. Muryn, H. Onishi and G. Thornton, Direct visualization of defect-mediated dissociation of water on  $\text{TiO}_2(110)$ , *Nat. Mater.*, 2006, **5**, 189–192.

94 T. Minato, Y. Sainoo, Y. Kim, H. S. Kato, K. Aika, M. Kawai, J. Zhao, H. Petek, T. Huang, W. He, B. Wang, Z. Wang, Y. Zhao, J. Yang and J. G. Hou, The electronic structure of oxygen atom vacancy and hydroxyl impurity defects on titanium dioxide (110) surface, *J. Chem. Phys.*, 2009, **130**, 124502.

95 H. Shi, Y.-C. Liu, Z.-J. Zhao, M. Miao, T. Wu and Q. Wang, Reactivity of the Defective Rutile  $\text{TiO}_2(110)$  Surfaces with Two Bridging-Oxygen Vacancies: Water Molecule as a Probe, *J. Phys. Chem. C*, 2014, **118**, 20257–20263.

96 Y. Zhang, Z. Xu, G. Li, X. Huang, W. Hao and Y. Bi, Direct Observation of Oxygen Vacancy Self-Healing on  $\text{TiO}_2$  Photocatalysts for Solar Water Splitting, *Angew. Chem., Int. Ed.*, 2019, **58**, 14229–14233.

97 H. Jeong and E. G. Seebauer, Influence of interstitial cluster families on post-synthesis defect manipulation and purification of oxides using submerged surfaces, *J. Chem. Phys.*, 2024, **161**, 121103.

98 H.-Y. Lee, S. J. Clark and J. Robertson, Calculation of point defects in rutile  $\text{TiO}_2$  by the screened-exchange hybrid functional, *Phys. Rev. B: Condens. Matter Mater. Phys.*, 2012, **86**, 75209.

99 K. L. Gilliard and E. G. Seebauer, Manipulation of native point defect behavior in rutile  $\text{TiO}_2$  via surfaces and extended defects, *J. Phys.: Condens. Matter*, 2017, **29**, 445002.

100 R. Nakamura, N. Ohashi, A. Imanishi, T. Osawa, Y. Matsumoto, H. Koinuma and Y. Nakato, Crystal-Face



Dependences of Surface Band Edges and Hole Reactivity, Revealed by Preparation of Essentially Atomically Smooth and Stable (110) and (100) n-TiO<sub>2</sub> (Rutile) Surfaces, *J. Phys. Chem. B*, 2005, **109**, 1648–1651.

101 R. Nakamura, T. Okamura, N. Ohashi, A. Imanishi and Y. Nakato, Molecular Mechanisms of Photoinduced Oxygen Evolution, PL Emission, and Surface Roughening at Atomically Smooth (110) and (100) n-TiO<sub>2</sub> (Rutile) Surfaces in Aqueous Acidic Solutions, *J. Am. Chem. Soc.*, 2005, **127**, 12975–12983.

102 Y. Nakabayashi and Y. Nosaka, OH Radical Formation at Distinct Faces of Rutile TiO<sub>2</sub> Crystal in the Procedure of Photoelectrochemical Water Oxidation, *J. Phys. Chem. C*, 2013, **117**, 23832–23839.

103 C. Haisch, C. Günemann, S. Melchers, M. Fleisch, J. Schneider, A. V. Emeline and D. W. Bahnemann, Irreversible surface changes upon n-type doping – A photoelectrochemical study on rutile single crystals, *Electrochim. Acta*, 2018, **280**, 278–289.

104 Y. Zhou and H. J. Fan, Progress and Challenge of Amorphous Catalysts for Electrochemical Water Splitting, *ACS Mater. Lett.*, 2021, **3**, 136–147.

105 M. Králik, Adsorption, chemisorption, and catalysis, *Chem. Pap.*, 2014, **68**, 1625–1638.

106 S. Carbonaro, M. N. Sugihara and T. J. Strathmann, Continuous-flow photocatalytic treatment of pharmaceutical micropollutants: Activity, inhibition, and deactivation of TiO<sub>2</sub> photocatalysts in wastewater effluent, *Appl. Catal., B*, 2013, **129**, 1–12.

107 X. Li, Y. Chen, Y. Tao, L. Shen, Z. Xu, Z. Bian and H. Li, Challenges of photocatalysis and their coping strategies, *Chem Catal.*, 2022, **2**, 1315–1345.

108 G. Singh, M. Kaur, V. Kumar Garg and A. C. Oliveira, Oxygen hyper stoichiometric trimetallic titanium doped magnesium ferrite: Structural and photocatalytic studies, *Ceram. Int.*, 2022, **48**, 24476–24484.

109 J. K. Grewal, M. Kaur, R. K. Sharma, A. C. Oliveira, V. K. Garg and V. K. Sharma, Structural and Photocatalytic Studies on Oxygen Hyperstoichiometric Titanium-Substituted Strontium Ferrite Nanoparticles, *Magnetochemistry*, 2022, **8**, 120.

110 S. J. Salih and W. M. Mahmood, Review on magnetic spinel ferrite (MFe<sub>2</sub>O<sub>4</sub>) nanoparticles: From synthesis to application, *Heliyon*, 2023, **9**, e16601.

111 O. A. Bulavchenko, O. S. Venediktova, T. N. Afonasenko, P. G. Tsyrul'Nikov, A. A. Saraev, V. V. Kachev and S. V. Tsybulya, Nonstoichiometric oxygen in Mn-Ga-O spinels: Reduction features of the oxides and their catalytic activity, *RSC Adv.*, 2018, **8**, 11598–11607.

112 Q. Yin, J. Kniep and Y. S. Lin, Oxygen sorption and desorption properties of Sr-Co-Fe oxide, *Chem. Eng. Sci.*, 2008, **63**, 2211–2218.

113 W. Li, B. Guan, X. Zhang, J. Yan, Y. Zhou and X. Liu, New mechanistic insight into the oxygen reduction reaction on Ruddlesden–Popper cathodes for intermediate-temperature solid oxide fuel cells, *Phys. Chem. Chem. Phys.*, 2016, **18**, 8502–8511.

114 A. J. Majewski, A. Khodimchuk, D. Zakharov, N. Porotnikova, M. Ananyev, I. D. Johnson, J. A. Darr, P. R. Slater and R. Steinberger-Wilckens, Oxygen surface exchange properties and electrochemical activity of lanthanum nickelates, *J. Solid State Chem.*, 2022, **312**, 123228.

115 S. Lian, L. He, C. Li, J. Ren, L. Bi, M. Chen and Z. Lin, Uncovering the Enhancement Mechanism of the Oxygen Reduction Reaction on Perovskite/Ruddlesden–Popper Oxide Heterostructures (Nd,Sr)CoO<sub>3</sub>/(Nd,Sr)₂CoO<sub>4</sub> and (Nd,Sr)CoO<sub>3</sub>/(Nd,Sr)₃Co<sub>2</sub>O<sub>7</sub>, *J. Phys. Chem. Lett.*, 2023, **14**, 2869–2877.

116 P. Erhart, K. Albe and A. Klein, First-principles study of intrinsic point defects in ZnO: Role of band structure, volume relaxation, and finite-size effects, *Phys. Rev. B: Condens. Matter Mater. Phys.*, 2006, **73**, 205203.

117 A. Janotti and C. G. Van de Walle, Native point defects in ZnO, *Phys. Rev. B: Condens. Matter Mater. Phys.*, 2007, **76**, 165202.

118 A. Goyal, P. Gorai, H. Peng, S. Lany and V. Stevanović, A computational framework for automation of point defect calculations, *Comput. Mater. Sci.*, 2017, **130**, 1–9.

119 A. A. Sokol, S. A. French, S. T. Bromley, C. R. A. Catlow, H. J. J. van Dam and P. Sherwood, Point defects in ZnO, *Faraday Discuss.*, 2007, **134**, 267–282.

120 R. Vidya, P. Ravindran, H. Fjellvåg, B. G. Svensson, E. Monakhov, M. Ganchenkova and R. M. Nieminen, Energetics of intrinsic defects and their complexes in ZnO investigated by density functional calculations, *Phys. Rev. B: Condens. Matter Mater. Phys.*, 2011, **83**, 45206.

121 J. L. Lyons, J. B. Varley, D. Steiauf, A. Janotti and C. G. Van de Walle, First-principles characterization of native-defect-related optical transitions in ZnO, *J. Appl. Phys.*, 2017, **122**, 035704.

122 R. A. Evarestov, A. Platonenko, D. Gryaznov, Y. F. Zhukovskii and E. A. Kotomin, First-principles calculations of oxygen interstitials in corundum: A site symmetry approach, *Phys. Chem. Chem. Phys.*, 2017, **19**, 25245–25251.

123 A. Platonenko, D. Gryaznov, Y. F. Zhukovskii and E. A. Kotomin, Ab initio simulations on charged interstitial oxygen migration in corundum, *Nucl. Instrum. Methods Phys. Res., Sect. B*, 2018, **435**, 74–78.

124 A. Kononov, C. W. Lee, E. P. Shapera and A. Schleife, Identifying native point defect configurations in  $\alpha$ -alumina, *J. Phys.: Condens. Matter*, 2023, **35**, 334002.

125 H. Y. Xiao, Y. Zhang and W. J. Weber, Stability and migration of charged oxygen interstitials in ThO<sub>2</sub> and CeO<sub>2</sub>, *Acta Mater.*, 2013, **61**, 7639–7645.

126 B. Medasani, M. L. Sushko, K. M. Rosso, D. K. Schreiber and S. M. Bruemmer, First-Principles Investigation of Native Interstitial Diffusion in Cr<sub>2</sub>O<sub>3</sub>, *J. Phys. Chem. C*, 2018, **122**, 12984–12993.

127 K. H. Yano, A. A. Kohnert, A. Banerjee, D. J. Edwards, E. F. Holby, T. C. Kaspar, H. Kim, T. G. Lach, S. D. Taylor, Y. Wang, B. P. Uberuaga and D. K. Schreiber, Radiation-Enhanced Anion Transport in Hematite, *Chem. Mater.*, 2021, **33**, 2307–2318.

128 A. Banerjee, E. F. Holby, A. A. Kohnert, S. Srivastava, M. Asta and B. P. Uberuaga, Thermokinetics of point defects in  $\alpha$ -Fe<sub>2</sub>O<sub>3</sub>, *Electron. Struct.*, 2023, **5**, 024007.

129 B. S. Thomas, N. A. Marks and B. D. Begg, Defects and threshold displacement energies in SrTiO<sub>3</sub> perovskite using atomistic computer simulations, *Nucl. Instrum. Methods Phys. Res., Sect. B*, 2007, **254**, 211–218.

130 B. Liu, V. R. Cooper, H. Xu, H. Xiao, Y. Zhang and W. J. Weber, Composition dependent intrinsic defect structures in SrTiO<sub>3</sub>, *Phys. Chem. Chem. Phys.*, 2014, **16**, 15590–15596.

131 S. A. Chambers, Y. Du, Z. Zhu, J. Wang, M. J. Wahila, L. F. J. Piper, A. Prakash, J. Yue, B. Jalan, S. R. Spurgeon, D. M. Kepaptsoglou, Q. M. Ramasse and P. V. Sushko, Interconversion of intrinsic defects in SrTiO<sub>3</sub>(001), *Phys. Rev. B*, 2018, **97**, 245204.

132 S. T. Murphy, M. W. D. Cooper and R. W. Grimes, Point defects and non-stoichiometry in thoria, *Solid State Ionics*, 2014, **267**, 80–87.

133 R. I. Palomares, M. T. McDonnell, L. Yang, T. Yao, J. E. S. Szymanowski, J. Neuefeind, G. E. Sigmon, J. Lian, M. G. Tucker, B. D. Wirth and M. Lang, Oxygen point defect accumulation in single-phase UO<sub>2+x</sub>, *Phys. Rev. Mater.*, 2019, **3**, 53611.

134 L. Yang and B. D. Wirth, Clustering of excess oxygen in uranium dioxide: A first-principles study, *J. Nucl. Mater.*, 2021, **554**, 153087.

135 X. M. Bai, Y. Zhang and M. R. Tonks, Strain effects on oxygen transport in tetragonal zirconium dioxide, *Phys. Chem. Chem. Phys.*, 2013, **15**, 19438–19449.

136 C. Jiang, X.-Y. Liu and K. E. Sickafus, First-principles prediction of the thermodynamic stability of xenon in monoclinic, tetragonal, and yttrium-stabilized cubic ZrO<sub>2</sub>, *Phys. Rev. B: Condens. Matter Mater. Phys.*, 2011, **83**, 52103.

137 A. Samanta, A theoretical study of the stability of anionic defects in cubic ZrO<sub>2</sub> at extreme conditions, *J. Mater. Sci.*, 2016, **51**, 4845–4855.

138 P. Ding, W. Li, H. Zhao, C. Wu, L. Zhao, B. Dong and S. Wang, Review on Ruddlesden–Popper perovskites as cathode for solid oxide fuel cells, *J. Phys.: Mater.*, 2021, **4**, 022002.

139 H.-Y. Lee and J. Robertson, Doping and compensation in Nb-doped anatase and rutile TiO<sub>2</sub>, *J. Appl. Phys.*, 2013, **113**, 213706.

140 A. Kyrtos, M. Matsubara and E. Bellotti, Migration mechanisms and diffusion barriers of vacancies in Ga<sub>2</sub>O<sub>3</sub>, *Phys. Rev. B*, 2017, **95**, 245202.

141 J. Meng, M. S. Sheikh, R. Jacobs, J. Liu, W. O. Nachlas, X. Li and D. Morgan, Computational discovery of fast interstitial oxygen conductors, *Nat. Mater.*, 2024, **23**, 1252–1258.

142 R. K. Behera, T. Watanabe, D. A. Andersson, B. P. Uberuaga and C. S. Deo, Diffusion of oxygen interstitials in UO<sub>2+x</sub> using kinetic Monte Carlo simulations: Role of O/M ratio and sensitivity analysis, *J. Nucl. Mater.*, 2016, **472**, 89–98.

